

Effect of Electromagnetic Ruler Braking (EMBr) on Transient Turbulent Flow in Continuous Slab Casting using Large Eddy Simulations

R. CHAUDHARY, B.G. THOMAS, and S.P. VANKA

Static electromagnetic braking (EMBr) fields affect greatly the turbulent flow pattern in steel continuous casting, which leads to potential benefits such as decreasing flow instability, surface defects, and inclusion entrapment if applied correctly. To gain a fundamental understanding of how EMBr affects transient turbulent flow, the current work applies large eddy simulations (LES) to investigate the effect of three EMBr ruler brake configurations on transient turbulent flow through the bifurcated nozzle and mold of a liquid-metal GaInSn model of a typical steel slab-casting process, but with deep nozzle submergence and insulated walls with no solidifying shell. The LES calculations are performed using an in-house graphic-processing-unit-based computational-fluid-dynamics code (LES-CU-FLOW) on a mesh of ~7 million brick cells. The LES model is validated first via ultrasonic velocimetry measurements in this system. It is then applied to quantify the mean and instantaneous flow structures, Reynolds stresses, turbulent kinetic energy and its budgets, and proper orthogonal modes of four cases. Positioning the strongest part of the ruler magnetic field over the nozzle bottom suppresses turbulence in this region, thus reducing nozzle well swirl and its alternation. This process leads to strong and focused jets entering the mold cavity making large-scale and low-frequency (<0.02 Hz) flow variations in the mold with detrimental surface velocity variations. Lowering the ruler below nozzle deflects the jets upward, leading to faster surface velocities than the other cases. The double-ruler and no-EMBr cases have the most stable flow. The magnetic field generates large-scale vortical structures tending toward two-dimensional (2-D) turbulence. To avoid detrimental large-scale, low-frequency flow variations, it is recommended to avoid strong magnetic fields across the nozzle well and port regions.

DOI: 10.1007/s11663-012-9634-6

© The Minerals, Metals & Materials Society and ASM International 2012

I. INTRODUCTION

ELECTROMAGNETIC braking (EMBr) is an efficient and nonintrusive way to control the turbulent flow pattern and its stability in the nozzle and the mold region of the continuous casting process for steel slabs. Turbulent flow in this process is the main cause of expensive defects, including surface quality, internal quality, and inclusion-related defects. As explained in more detail elsewhere,^[1,2] surface defects caused by meniscus freezing arise if the surface flow near the slab-metal interface is too slow to prevent hook formation and to provide convective mixing to help melt the mold powder. Slag entrainment defects will occur if the flow is too fast or the liquid profile is not flat enough. Finally, and most importantly, intermittent defects of many

kinds may occur as a result of excessive transient fluctuations in the liquid level.

Flow is controlled by the nozzle and mold geometry, casting speed, nozzle submergence depth, argon gas injection, and the application of electromagnetic forces.^[1] Electromagnetic forces are applied optionally as either static or moving magnetic fields through the thickness of the strand. Static (direct current [DC]) electromagnetic fields induce current in the conducting liquid steel, which in turn, generates forces that oppose the flow directly, so are they referred to as “brakes” or “EMBr.”^[3] EMBr fields include local cylindrical-shaped fields, wide “ruler-shaped” magnetic fields across the entire mold width, and double-ruler fields, which are sometimes referred to as flow-control, or “FC-mold” fields.^[4] Moving (alternating current [AC]) fields originated with electromagnetic stirring (EMS), where moving the fields in opposite directions on opposite sides of the strand induces rotating flow, usually in the transverse plane in the mold (Mold-EMS)^[5,6] or electromagnetic rotary stirring (EMRS).^[7,8] Moving the fields in the same direction, which is sometimes called “multimode EMS,” can induce accelerating flow (electromagnetic level accelerator (EMLA)) or decelerating flow (electromagnetic level stabilizer (EMLS)).^[7,8] Electromagnetic forces offer an advantage over other flow-control

R. CHAUDHARY, PhD Student, Department of Mechanical Science & Engineering, University of Illinois at Urbana—Champaign, Urbana, IL 61801, is now with Global General Motors R&D, India Science Lab, GM Tech Centre (India), Bangalore 560066, India. Contact e-mail: rchaudh4@illinois.edu B.G. THOMAS and S.P. VANKA, Professors, are with the Department of Mechanical Science & Engineering, University of Illinois at Urbana—Champaign.

Manuscript submitted November 22, 2011.

parameters because the induced force varies with the strength of the liquid metal flow, giving the system the theoretical ability to be self-stabilizing for turbulent flow variations. In practice, this is difficult to achieve.

The effect of electromagnetics can be studied with plant experiments^[4], measurements in liquid-metal models such as mercury^[5,9] or GaInSn^[10,11], and computational models. Previous computational studies have focused mainly on the influence of static electromagnetic braking on the time-averaged flow pattern using steady Reynolds-averaged Navier-Stokes (RANS) computational models.^[3,4,12–15] A few studies have applied transient models such as large eddy simulation (LES)^[16–18] and unsteady RANS (URANS)^[18,19] to analyze turbulent flow variations in the process without EMBr. The study of transient flow effects of EMBr is relatively rare.^[20–22]

Qian and Wu^[20] employed LES to study the effects of EMBr, submerged entry nozzle (SEN) depth, and port angle on flow and vortex formation in continuous slab casting. Electromagnetic braking across the free surface was found to suppress turbulence and biased vortices significantly. Kageyama and Evans^[21] developed a similar coupled LES-electromagnetic field-free surface model. The model performed reasonably well in several physical problems such as two-dimensional (2-D) cavity flow and flow of mercury in a pool intended to simulate electromagnetic casting; however, the usage for any practical investigative study was left for the future. Miki and Takeuchi^[22] applied LES to find that unbalanced flow from turbulent variations was responsible for bubble and inclusion entrapment, and it was reduced by a double-ruler brake (“FC-mold”).

Previous LES models have been constrained by slow computational speed and used relatively coarse grids with classic subgrid scale models, such as Smagorinsky and no wall treatment. The detailed effects of EMBr on the turbulence and flow structures have not been studied, and there is insufficient validation with measurements. The current work applies a LES model with a wall-adaptive local eddy (WALE) viscosity model on a fine mesh (~7 million cells) with an accurate Werner-Wengle wall treatment. This model was found to be the best in a previous study of the accuracy and efficiency of various transient and steady models of this system without EMBr.^[18] The model is first rigorously validated with velocity measurements in a small-scale GaInSn model using ultrasonic Doppler velocimetry (UDV) before using it to investigate the effect of electromagnetic braking on the turbulent flow behavior.

This work extends the previous study^[18] of time-averaged and transient flow in the continuous-casting nozzle and mold to investigate the effects of single- and double-ruler EMBrs and their locations on the turbulent flow. Specifically, the time average flow, turbulent kinetic energy (TKE), TKE budgets, Reynolds stresses, instantaneous flow, and proper orthogonal decomposition (POD) analysis are evaluated to understand the effect of electromagnetic braking on turbulent flow. Practical insights are revealed for the design and location of ruler brakes to stabilize the turbulent flow and to decrease the associated defects in the continuous casting process.

II. MODEL CASTER GEOMETRY

The current work investigates turbulent flow in a small-scale liquid metal GaInSn physical model of the continuous steel-slab casting process at Forschungszentrum Dresden-Rossendorf (FZD), Dresden, Germany, where velocity measurements have been performed in previous works,^[10,11,23] including the effects of EMBr.^[10,11] Subsequent details on the physical GaInSn model and the measurements can be found in Timmel *et al.*^[10,11,23] and in Chaudhary *et al.*^[18] An ultrasonic velocity profiler was used to measure instantaneous horizontal velocity histories at various vertical positions across the midplane along different horizontal lines. The GaInSn model of the mold region has 140 mm (width) × 35 mm (thickness) × 300 mm (height) and vertical walls. The model features a 300-mm-long cylindrical inlet nozzle with 10-mm inner bore diameter, a well-shaped bottom, and 0-deg (horizontal) angled bifurcated ports with port-to-bore ratio of 3.31. Figures 1(a) through (c) show the schematics of this facility with front, side, and bottom views, respectively. The “orange” rectangle in the front-view midplane slice shows the approximate location of the magnetic coil for the single-ruler brake (case 2) with the maximum field strength located at 92 mm below the top free surface of the liquid. Table I contains the geometric details, casting conditions, physical properties of GaInSn, and the EMBr conditions. Measurements were performed for the first three cases.

III. COMPUTATIONAL MODEL

A. Fluid Flow

The LES model developed for this work solves the following three-dimensional filtered continuity equation and filtered time-dependent Navier-Stokes (N-S) equations^[24,25]:

$$\frac{\partial u_i}{\partial x_i} = 0 \quad [1]$$

$$\frac{\partial u_i}{\partial t} + \frac{\partial u_i u_j}{\partial x_j} = -\frac{1}{\rho} \frac{\partial p^*}{\partial x_i} + \frac{\partial}{\partial x_j} \left((\nu + \nu_s) \left(\frac{\partial u_i}{\partial x_j} + \frac{\partial u_j}{\partial x_i} \right) \right) + \frac{1}{\rho} F_i \quad [2]$$

where u_i are filtered velocity components; F_i is the filtered Lorentz force caused by the magnetic field, described in Section III-B; and p^* is “modified” static pressure. Theoretically, the real static pressure field p could be found from $p^* - \frac{2}{3} \rho k_r$, where k_r is an unknown residual kinetic energy. The two pressure fields are likely similar for the current fine-grid simulations. To account for details of the flow pattern that are too small to resolve with the computational grid, the WALE model^[26] was applied to define the subgrid scale viscosity, (ν_s)

$$\nu_s = L_s^2 \frac{(S_{ij}^d S_{ij}^d)^{3/2}}{(S_{ij} S_{ij})^{5/2} + (S_{ij}^d S_{ij}^d)^{5/4}} \quad [3]$$

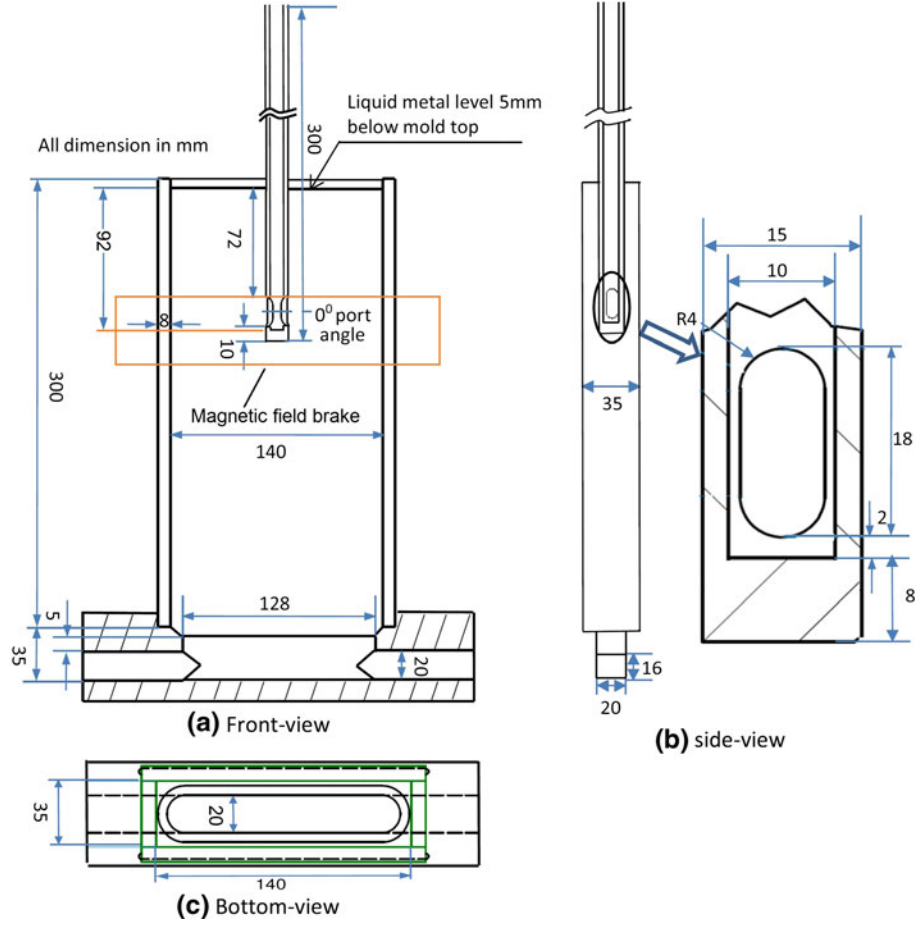


Fig. 1—Geometry of GaInSn model^[10,11,23] of continuous caster with rectangle to show case 2 single-ruler EMBR coil location.

Table I. Process Parameters

Volume flow rate/nozzle bulk inlet velocity	110 mL/s/1.4 m/s
Casting speed	1.35 m/min
Mold width	140 mm
Mold thickness	35 mm
Mold length	330 mm
Total nozzle height	300 mm
Nozzle port dimension	8 mm (width) × 18 mm (height)
Nozzle bore diameter (inner/outer)	10 mm/15 mm
SEN submergence depth (liquid surface level to top of port)	72 mm
Density (ρ)	6360 kg/m ³
Viscosity (μ)	0.00216 kg/m s
Electrical conductivity (σ)	3.2×10^{06} (1/(ohm m))
Nozzle port angle	0 deg
Solidifying shell	No
Gas injection	No
EMBr cases	1. No EMBR 2. 92-mm single ruler 3. 121-mm single ruler 4. Double ruler

where, $S_{ij} = \frac{1}{2} \left(\frac{\partial u_i}{\partial x_j} + \frac{\partial u_j}{\partial x_i} \right)$, $S_{ij}^d = \frac{1}{2} (g_{ij}^2 + g_{ji}^2) - \frac{1}{3} \delta_{ij} g_{kk}^2$, $g_{ij} = \frac{\partial u_i}{\partial x_j}$ where, $\delta_{ij} = 1$, if $i=j$, else $\delta_{ij} = 0$. As the grid is refined, accuracy improves to approach that of a direct numerical simulation because v_s approaches zero as a result of the dependency of coefficient L_s on grid size $L_s = C_w(\Delta x \Delta y \Delta z)^{1/3}$, $C_w^2 = 10.6 C_s^2$, $C_s = 0.18$, Δx , Δy , and Δz are the grid spacing in x , y , and z directions.

B. Magnetohydrodynamic (MHD) Equations

In many MHD processes with flowing liquid metal, the induced magnetic field is negligible compared with the externally applied magnetic field.^[27] This finding was shown to include continuous casting of steel.^[4] Thus, Ohm's law can be combined with conservation of current to derive a Poisson equation for the electric potential ϕ , which can then be used, given the coupled instantaneous velocity field $\vec{v} = u_i$, and the external applied magnetic field \vec{B}_0 , to calculate the body force $\vec{F}_L = F_i$ for the source term in Eq. [2] as follows^[27]:

$$\vec{F}_L = \vec{J} \times \vec{B}_0 \quad [4]$$

$$\vec{J} = \sigma (-\nabla \phi + \vec{v} \times \vec{B}_0) \quad [5]$$

$$\nabla^2 \phi = \nabla \cdot (\vec{v} \times \vec{B}_0) \quad [6]$$

where \vec{J} is the current density (Amp/m²) and \vec{B}_0 is the external magnetic field (Tesla), given as $\vec{B}_0 = (B_{0x} = 0.0, B_{0y}(\vec{x}), B_{0z} = 0.0)$. Here B_{0y} is one of the magnetic fields shown in Figure 2 that was applied normal to the wide faces and was both measured and calculated for the GaInSn model in previous work.^[10,11]

The preceding coupled governing equations of LES for incompressible-MHD flows with small-induced fields (magnetic $Re < 1$) have been solved in our in-house graphic processing unit (GPU) based code (LES-CU-FLOW^[18,28,29]). Details of the numerical methodology, boundary conditions, and meshes were presented previously^[18] but are summarized briefly in the next two sections.

C. Computational Domain, Mesh, and Boundary Conditions

The computational domain used in the LES calculations is given in Figure 1. To avoid complications in creating brick mesh, the bottom region of the mold is approximated with an equal-area rectangle, as explained

in Reference 18. Additional details and process parameters are given in Table I.

The mesh consists of ~ 7 million ($384 \times 192 \times 96$) brick cells and is shown in Reference 18. To increase computational efficiency, the long nozzle bore was truncated at the top free surface of the liquid metal, and the inlet boundary conditions were copied from down the nozzle to achieve fully developed turbulent flow in the short nozzle pipe length of $L/D \sim 7.2$. This inlet mapping condition was found to perform well, and its details are explained elsewhere.^[18,30] The top free surface in the mold is a free-slip boundary with zero normal velocity and zero wall-normal derivatives of tangential velocities. All other solid walls of the domain are considered no-slip (zero velocity) and the Werner-Wengle wall treatment was used.^[18,31] The mold outlet was trimmed in the forward flow region at the narrow faces and a convective outlet boundary condition was used, which conserves mass at each instant according to the turbulent flow-rate fluctuations.^[18,32] Additional details are given in Reference 18. For the MHD equations, all the boundaries were considered insulated with normal current zero, which leads to the following Neumann boundary condition at the walls for electric potential^[28]:

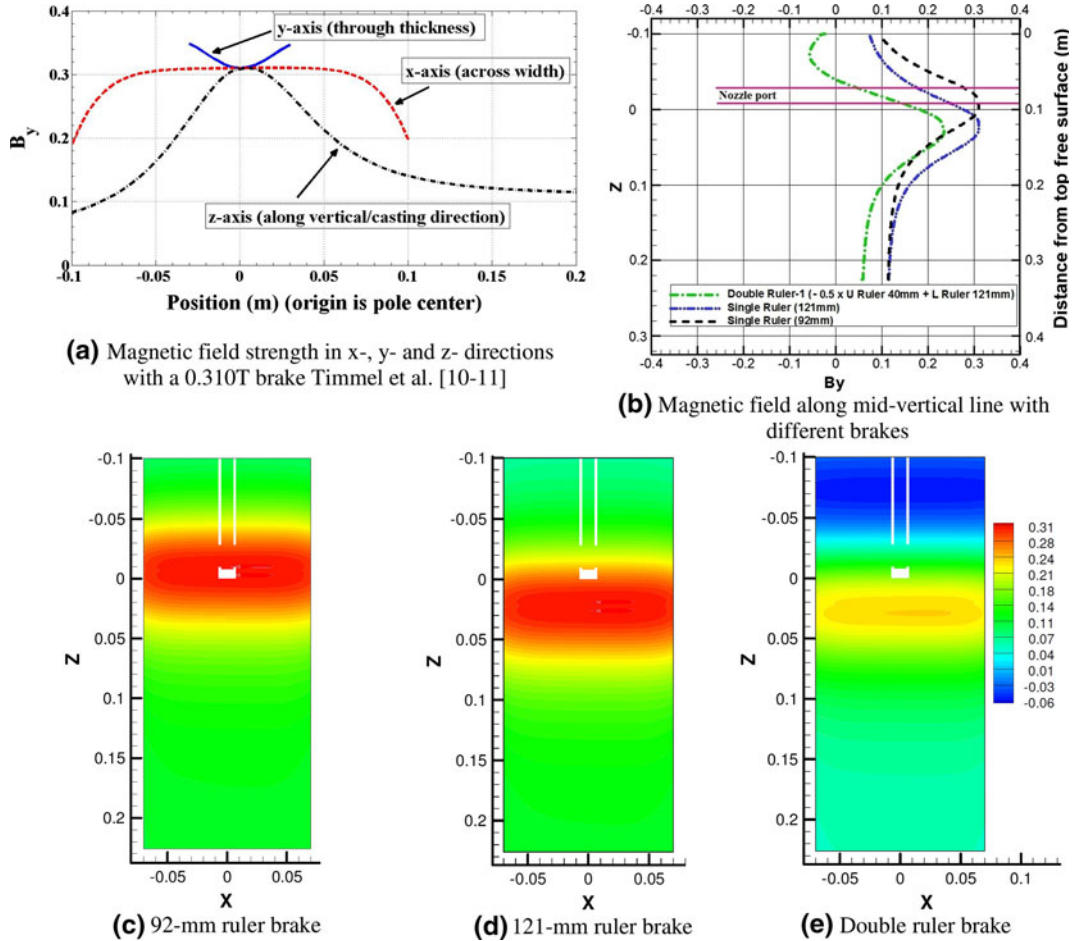


Fig. 2—Magnetic field strength distributions showing (a) variation in three coordinate directions. (b) Profiles along the midvertical line for different brakes relative to nozzle ports (c) through (e) midplane contours with the three ruler brakes.

$$\frac{\partial \phi}{\partial n} = 0 \quad [7]$$

where n is the unit normal to the boundary. This condition matches the insulating plastic walls of the physical model but differs from a real continuous caster, where the liquid is contained in a solid steel shell that conducts current.

D. Numerical Method and Computational Cost

The coupled filtered N-S-MHD equations (Eqs. [1] through [6]), were discretized using the finite-volume method on a structured Cartesian staggered grid. Detailed steps of the method are outlined in Chaudhary *et al.*^[18,28,29] A geometric multigrid solver is used to solve the pressure Poisson equation (PPE) and electric potential Poisson equation (EPPE) (Eq. [6]). The Lorentz force is added as an explicit source into the momentum equations. Each turbulent flow simulation with EMBr is initiated from the results of a 49.14-second simulation without EMBr, that was started from zero velocity. For each simulation, the flow field is allowed to develop for ~5 seconds before starting to collect mean velocities for ~3 seconds (50,000 timesteps, $\Delta t = 0.00006$ seconds). Once the mean velocities stabilize, they are collected together with Reynolds stresses and TKE budget terms for another ~25 seconds.

The computations were performed on a personal computer with a 2.66 GHz Intel Xeon processor (Intel Corp., Santa Clara, CA), 8.0 GB RAM, and a NVIDIA C1060 GPU with 4 GB memory. The LES-CU-FLOW model with MHD required ~20 days for each of the three EMBr simulations (*i.e.*, ~33 seconds total time or ~550,000 timesteps simulated in each run). The time needed with EMBr is approximately double that with no EMBr^[18] because it requires the solution of EPPE, which is the most computationally intensive step, similar to PPE and current density equations.

IV. ELECTROMAGNETIC BRAKE CONFIGURATIONS

The current work investigates the effect of static (DC) EMBr via four different cases, as given in Table I. The first three cases, including flow with no EMBr, have measurement data for horizontal velocities provided by Timmel *et al.*^[10,11,23] Cases 2 and 3 are single-ruler brake configurations, with the maximum field intensity at midplane located at different distances below the top liquid surface (92 mm and 121 mm). The final case 4 is a double-ruler brake, which is typical of that used in commercial application, where it is known as Flow-Control or “FC-mold” EMBr (ABB), and has only model predictions.

Figure 2(a) presents the strength of the magnetic field in all three directions of the 0.310T single-ruler brake.^[10,11] Here, 0.310T is the strength of the magnetic field at its “pole center,” whereas the maximum of 0.33T is found at the wideface wall centerlines. The origin in this figure on the horizontal axis signifies the location of the

pole center of the brake. The magnetic field is relatively constant across the width but changes significantly in the vertical and thickness directions. The field is strongest at the pole in the vertical direction but weakest at the pole in the thickness direction. The ruler-shaped field for case 2 shown in Figure 2(a) is called the 92-mm EMBr case when the pole center is located 92 mm below the liquid surface at the center of the mold.

Figure 2(b) compares the variation of the magnetic field strengths of all three brakes along the midvertical (z) axis. The left y -axis of this double y plot is z distance relative to the free surface at -100 mm, whereas the right y -axis is the distance below the top free-surface liquid level in the mold. The 121-mm ruler brake was generated by simply displacing the 92-mm brake field downward by 29 mm. To generate the double-ruler brake, an upper braking field was subtracted from a lower braking field, chosen to be the 121-mm brake. This upper brake was generated by taking half of the field strength profile in Figure 2(a) and displacing it upward to put its pole center at 40 mm from the top surface. Because the fields in the double-ruler brake are in opposite directions, they cancel partially so the field is weaker near the nozzle port region and below. The negative upper ruler also makes the magnetic field in the upper region of the double-ruler brake in the opposite (negative) direction, compared to all the other fields. The relative strengths in the Figure 2(b) profiles are also compared as contours in the x - z midplane in Figures 2(c) through (e).

V. COMPARISON OF MODEL PREDICTIONS WITH MEASUREMENTS

Time-averaged horizontal velocity contours from LES-CU-FLOW are compared in Figure 3 with UDV measurements at the mold midplane for the first three cases. The LES predictions match well with no EMBr (Figure 3(a)) and are also reasonable for both single-ruler EMBr cases (Figures 3(b) and (c)). As documented in previous work^[18] and as stated by Timmel *et al.*,^[10,11,23] the measurements close to the SEN and close to the narrow face are inaccurate, likely because of interaction effects near walls and vertical spatial resolution. The measurements also show wiggles due to the small number of frames included in the time average (~125 total frames over ~25 seconds in no-EMBr and 92-mm EMBr cases and ~51 frames for ~10 seconds in 121-mm EMBr case) compared with the LES predictions (~466,666 frames over 28 seconds). This problem is also likely responsible for the lower velocities at the center of the jet, which is physically unrealistic.

To assess the model predictions further, the time-average predictions of horizontal velocity are compared in Figure 4 with measurements along three lines (95, 105, and 115 mm from the mold top). The quantitative match is good, except close to the narrow face (NF) and SEN (see the 95-mm line), where the measurements are inaccurately low. The predictions for the 121-mm ruler brake are the most different likely as a result of insufficient averaging time. The overall agreement is striking, both in qualitative behavior and in quantitative

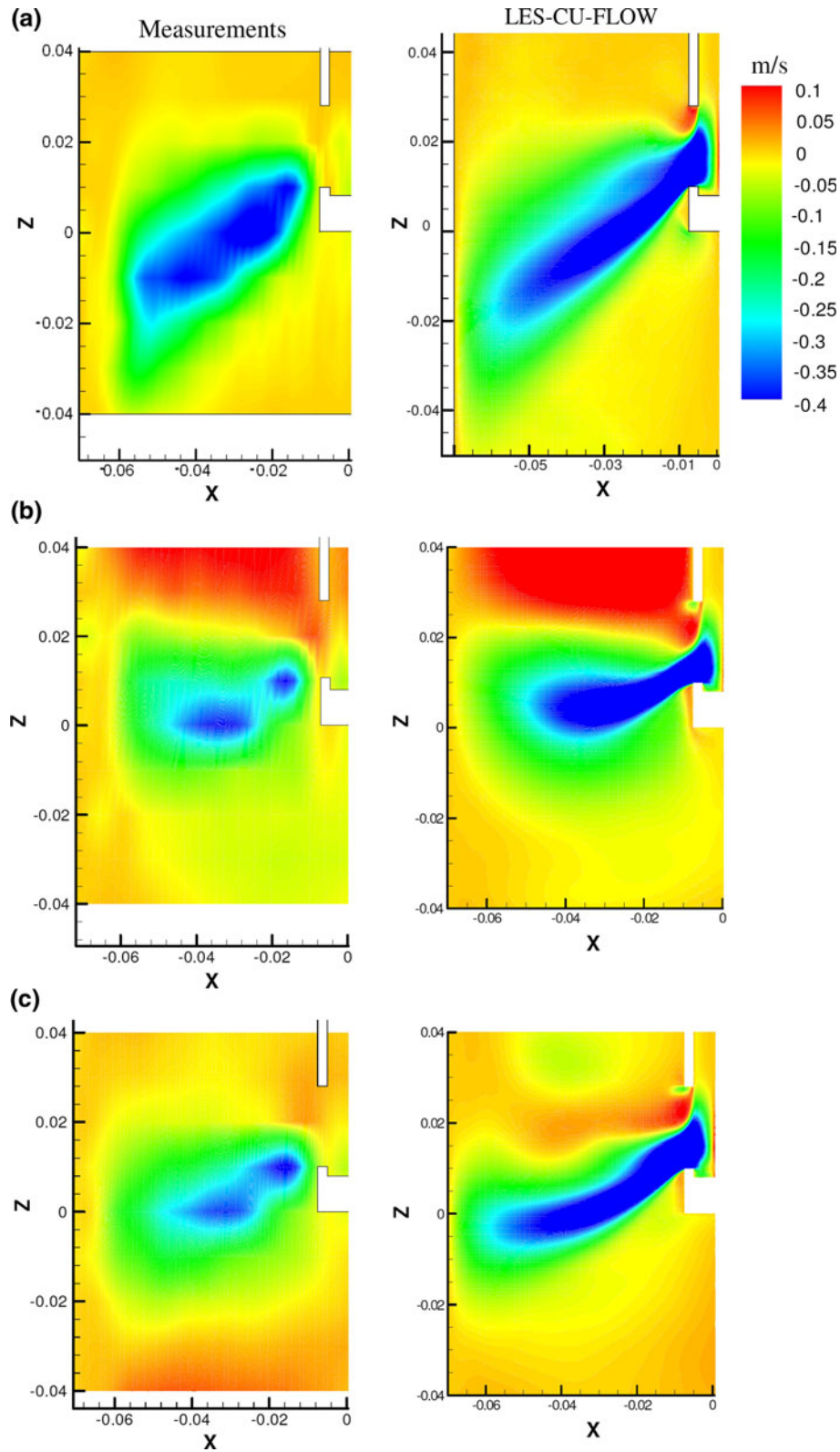


Fig. 3—Time-averaged horizontal velocity contours comparing LES-CU-FLOW predictions and ultrasonic Doppler velocimetry measurements^[10,11,23] with (a) no-EMBr, (b) single-ruler brake across nozzle (EMBr) centered 92 mm below free surface, and (c) single-ruler brake below nozzle (EMBr) centered 121 mm below the free surface (Color figure online).

values. The features in common between the predictions and measurements reveal several important new insights.

Both the model predictions and measurements show that applying either of the ruler brakes causes the time-average jet to bend upward, especially for the 92-mm

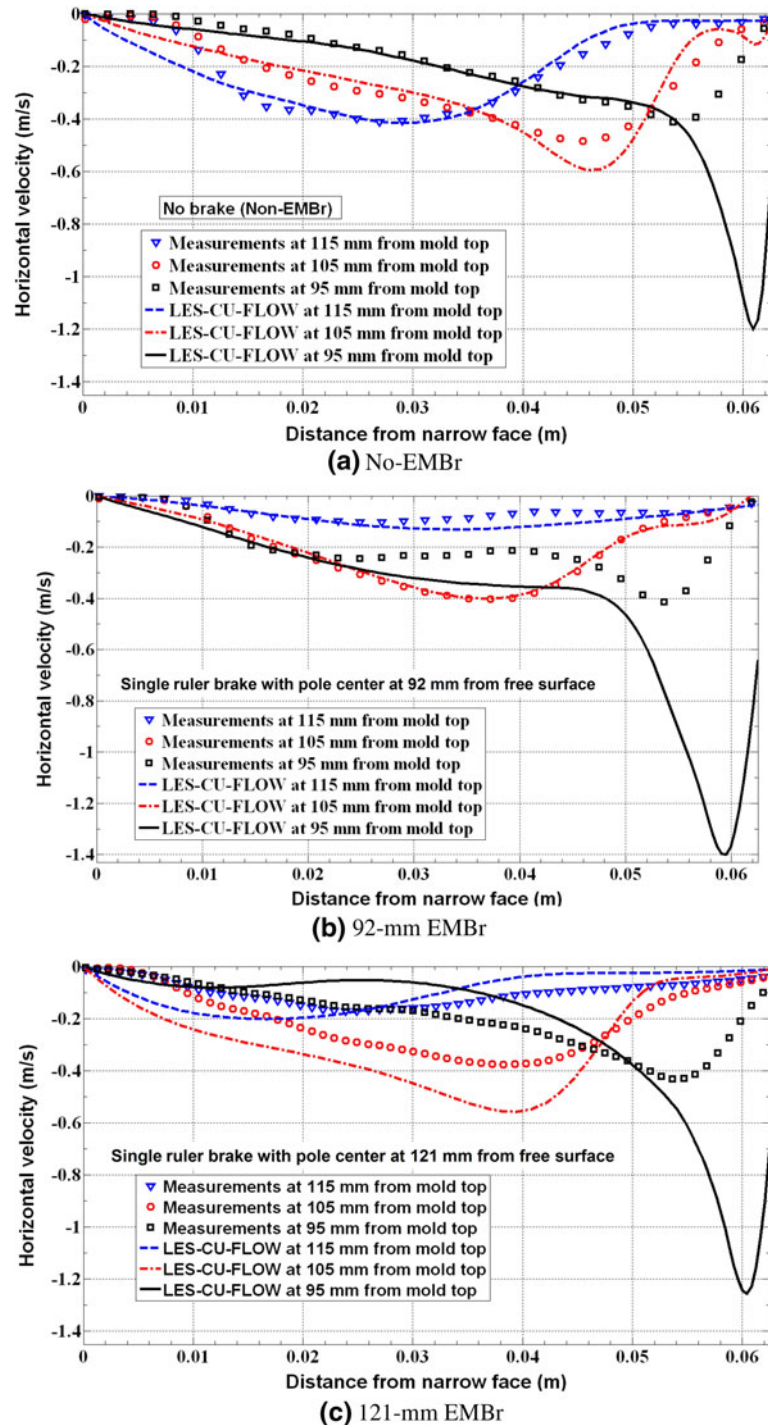


Fig. 4—Effect of EMBR on time-average horizontal velocity profiles, comparing LES-CU-FLOW and UDV measurements.^[10,11,23]

brake, and to impinge higher on the narrow face. The brakes also slow down the jet slightly. Strong reverse velocity regions (which is shown in red in Figure 3) are observed just above the jet with the 92-mm brake, and slight reverse velocity is observed just below the jet with 121-mm brake. Reversed-flow so near above the jet is not observed without EMBR and has not been found with previous models. This observation is explained in the results sections.

A comparison of the model predictions with measurements of transient horizontal velocities at a typical point in the jet in the mold midplane (P-4 in Figure 5) is presented in Figure 6 for 12 seconds of data. As shown previously in Reference 18, the measurements have ~0.2 seconds temporal filtering so the higher frequencies cannot be captured. This measurement limitation can be viewed clearly in Figure 6. Applying 0.2 seconds moving time average and appropriate spatial averaging to the

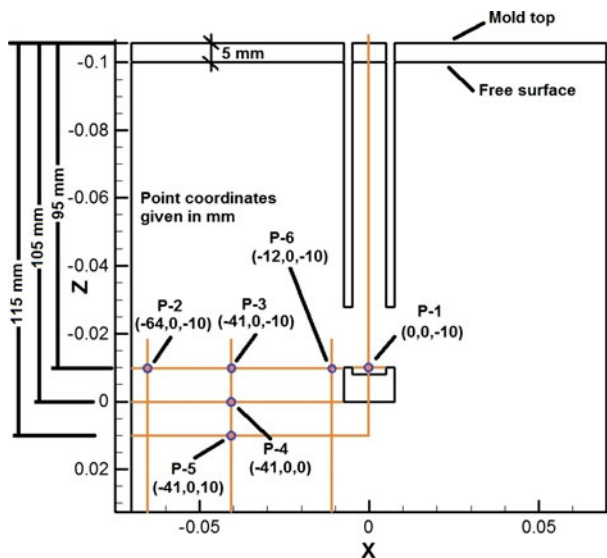


Fig. 5—Location of points in mold midplane where instantaneous velocity histories are presented.

predictions enables them to match well with the variations in the measured signals. Spatial averaging alone was found to have a negligible effect.^[18] Large, low-frequency variations are observed in each of the predicted and measured signals, especially for the 92-mm EMBR case.

Comparisons made at several other points (P-2, P-3, and P-5) produced similar close agreement in transient behavior of the filtered predictions and the measurements, considering that the chaotic turbulent flow histories are never exactly reproducible. Figure 7(a) shows the unfiltered velocity predictions at point P-2, which is located near the narrow-face wall. At this location beyond and above the jet region, both the velocities and their variations are all very small, especially for the no-EMBr case, which is very stable. With EMBr, sharp velocity spikes are sometimes observed, especially for the 92-mm EMBr case.

Figure 7(b) compares unfiltered velocity predictions at points P-3 and P-5 for the no-EMBr, 92-mm, and 121-mm EMBr cases. At these locations inside the jet, the velocities are always high and variable. Without EMBr, the velocity also always exhibits a strong high-frequency component. With EMBr, the high-frequency component is observed only in the jet center (P-3 and P-4). At points above (P-3) and below (P-5) the jet, the magnetic brake filters out the high-frequency turbulence, which is responsible for the high-frequency fluctuations, so the signals are smoother. Large, low-frequency variations (>2 -second period) persist, especially for the 92-mm brake, as discussed in detail later. Overall, the LES predictions match well with the measurements for both time-average and instantaneous velocities.

VI. TIME-AVERAGED RESULTS

Having validated the LES model, its predictions of velocity, turbulence, flow structures, Reynolds stresses,

and turbulent kinetic energy transport in the nozzle and mold were evaluated for four cases. The effects of electromagnetic braking on both the time-averaged and instantaneous flow structures in the liquid-metal caster model are investigated, based on ~49 seconds of simulation results for non-EMBr case and ~33 seconds of simulation results for EMBr cases (starting with no-EMBr instantaneous results at 49 seconds).

A. Nozzle Flow

The time-averaged velocity magnitude and vectors are compared in the nozzle midplane bottom regions for the four cases in Figure 8. The corresponding port outlet velocity magnitude profiles along the vertical centerlines on both sides are shown in Figure 9. The flow fields are symmetric between the right and left sides in this region, indicating that 28 seconds is enough time to provide a representative average for the high-frequency turbulent fluctuations that dominate the velocity variations in this. The jet from the weaker magnetic field cases is thicker, steeper downward, and shows more vertical spread. Applying stronger magnetic fields within the nozzle bottom, the two single-ruler cases, especially 92-mm EMBr, show thinner, shallower, and straighter jets. Such jets become highly unstable after entering the mold cavity. Similar jet behavior was found with a mountain-bottom nozzle,^[33] relative to the well-bottom nozzle that is also used in the current work. The effect of the nozzle bottom flow behavior on the mold flow is presented in the sections that follow.

B. Mold Flow

The predicted time-averaged velocity magnitude contours and vectors are compared in Figure 10. With no EMBR, the average flow is symmetric between sides. Near the SEN, this symmetry is achieved within 1 to 2 seconds of time averaging because of the dominance of high-frequency turbulent flow variations.

With the 92-mm ruler brake, the jet shows strong right-left asymmetry in the time-average flow field even after 28 seconds. The strong magnetic field at the nozzle bottom suppresses high-frequency turbulence strongly, which allows small differences in the low-frequency variations of the two jets exiting the ports to persist into the mold where they form long-lasting, large-scale flow structures. The jets in this case form a roll on one side while hitting the narrow face wall on the other, sending flow straight upward and downward. The slight asymmetry in the magnetic field (Figure 2) was ruled out from being responsible for the huge flow variations by performing a ~48-second simulation with a perfectly symmetric magnetic field, and again observing asymmetric flow. Because of the time consuming time averaging in these simulations, a rather coarse mesh (~0.8 million brick cells) was then used with perfectly symmetric magnetic field to ascertain the time period of this asymmetry. The flow field resulted in an almost symmetrical time-averaged flow field in ~200 seconds with circular rolls on each side similar to the left side of Figure 10 in the 92-mm EMBR case. These results

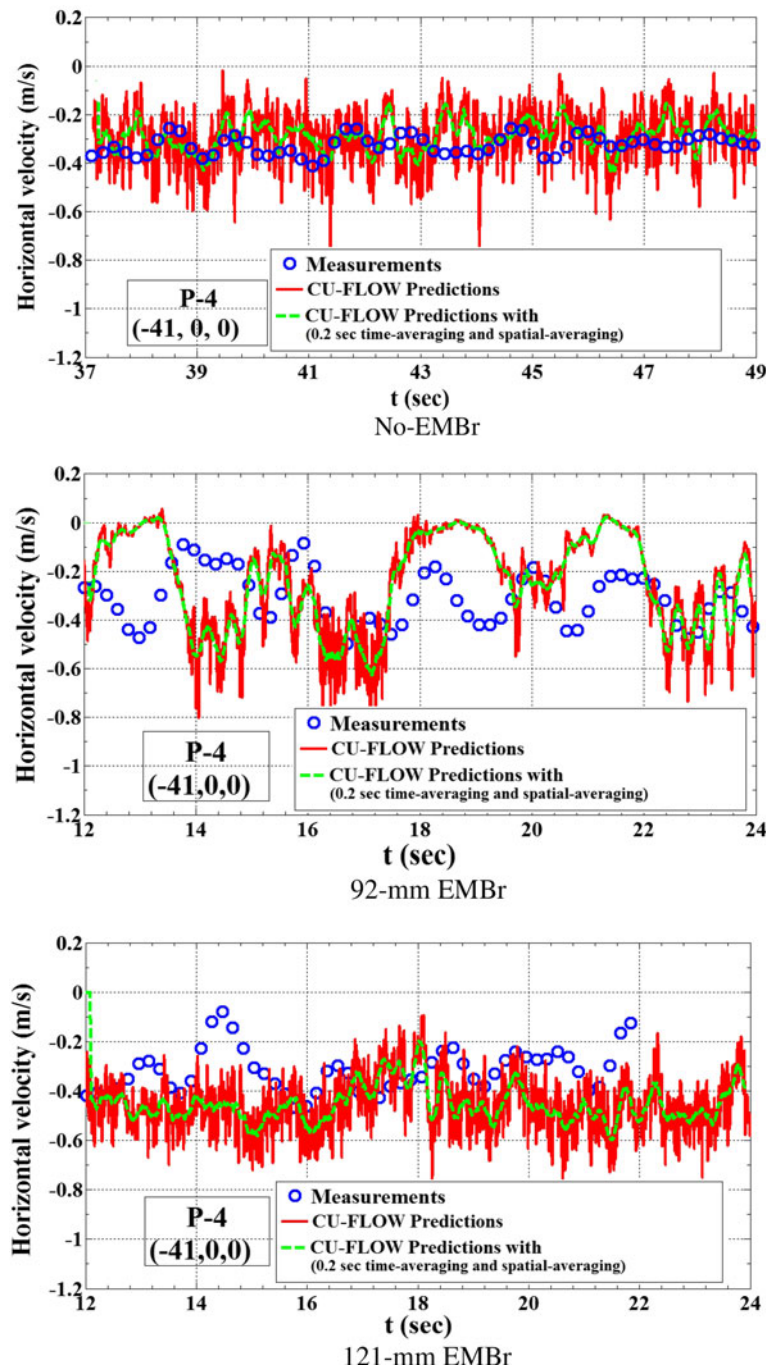


Fig. 6—Transient horizontal velocity comparing LES-CU-FLOW predictions and measurements^[10,11] at point 4 in mold midplane (shown in Fig. 5).

suggest that the strong magnetic field in the nozzle bottom is responsible for the large scales and long time variations of the detrimental persistently asymmetric flow. In addition, slight asymmetries in the magnetic field might aggravate the instabilities and extend the time scales of the unstable flow.

With the lower 121-mm EMBR ruler case, the weaker magnetic field in the nozzle bottom makes flow relatively more turbulent in the nozzle. The jets then exit the ports with a shallower downward angle. They are deflected upward even more by the EMBR field and consistently

impinge almost horizontally onto the narrow faces, sending strong upward flows toward the top surface and a classic double-roll flow pattern. This produces the fastest surface velocity of all the cases.

With the double-ruler brake, the magnetic field is weakest at the nozzle bottom, so the flow retains more turbulence (similar to the no-EMBr case). With a perfectly symmetric double-ruler brake, the flow achieved symmetry within ~26 seconds. This case thus produces turbulence scales that are much smaller than with 92 mm EMBR but bigger than with 121 mm

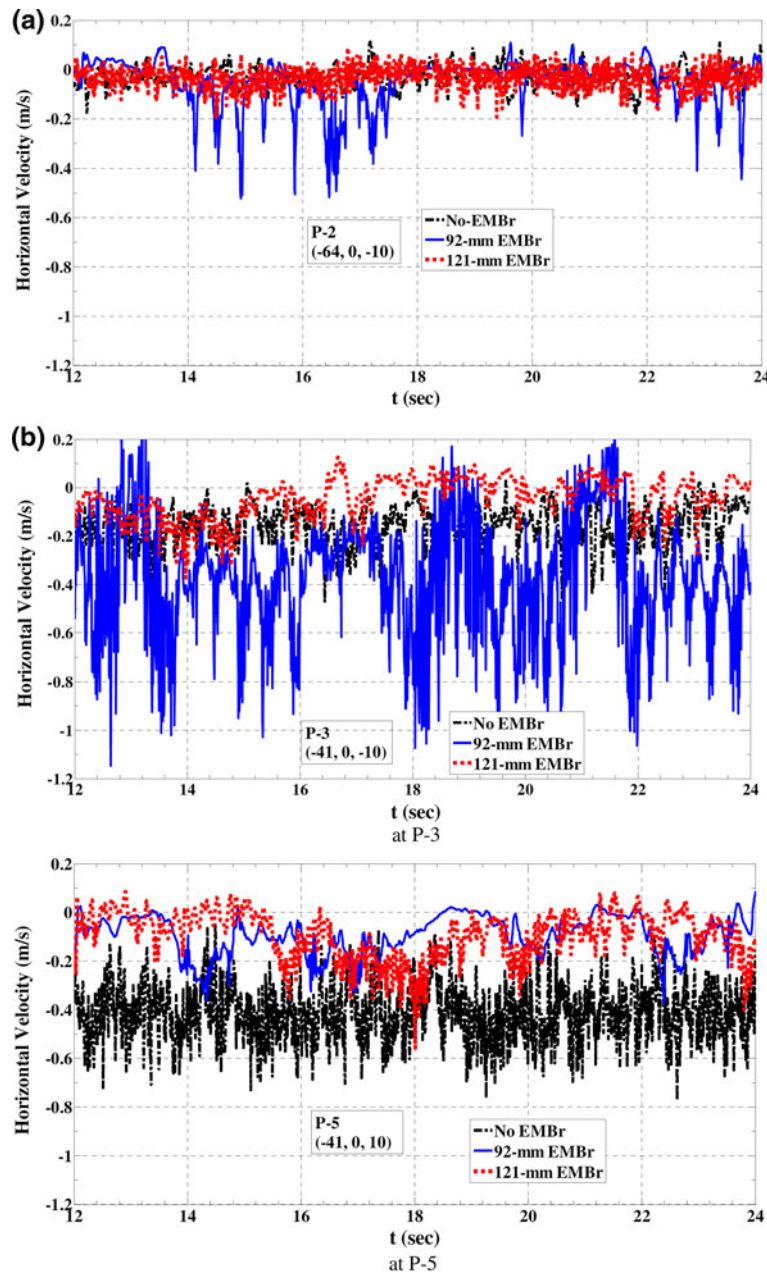


Fig. 7—(a) Unfiltered transient horizontal velocity predictions at point 2 in mold midplane (shown in Figure 5). (b) Unfiltered transient horizontal velocity predictions at point 3 and point 5 (shown in Fig. 5) in mold midplane in no-EMBr, 92-mm, and 121-mm EMBR cases.

EMBr. The jets are angled downward, similar to those without EMBR, so the double-ruler brake produces large, strong flow structures below the nozzle bottom and weak flow in the upper zone. The upper EMBR field further decreases the magnitude of surface-directed flows.

C. Surface Flow

The horizontal “surface” velocity below the top free surface is presented in Figure 11(a). As explained previously, the surface flow is of great practical importance to the commercial continuous-casting process. This GaInSn model has a deep submergence relative to a

typical caster so it tends to have much slower surface flows. The no-EMBr case would, thus, likely be prone to meniscus freezing and related defects. Applying the 121 mm EMBR increases surface velocity significantly and thus could act as an effective, nonintrusive, easily adjustable method to increase free surface velocity as needed to decrease meniscus freezing defects. The other two EMBR configurations produce surface velocity between the no-EMBr and 121-mm EMBR cases. The upward flow velocity at 35 mm below the free surface shown in Figure 11(b) is consistent with controlling the surface flow. The 121-mm EMBR case has the highest upward and downward velocities close to the narrow faces and nozzle, respectively.

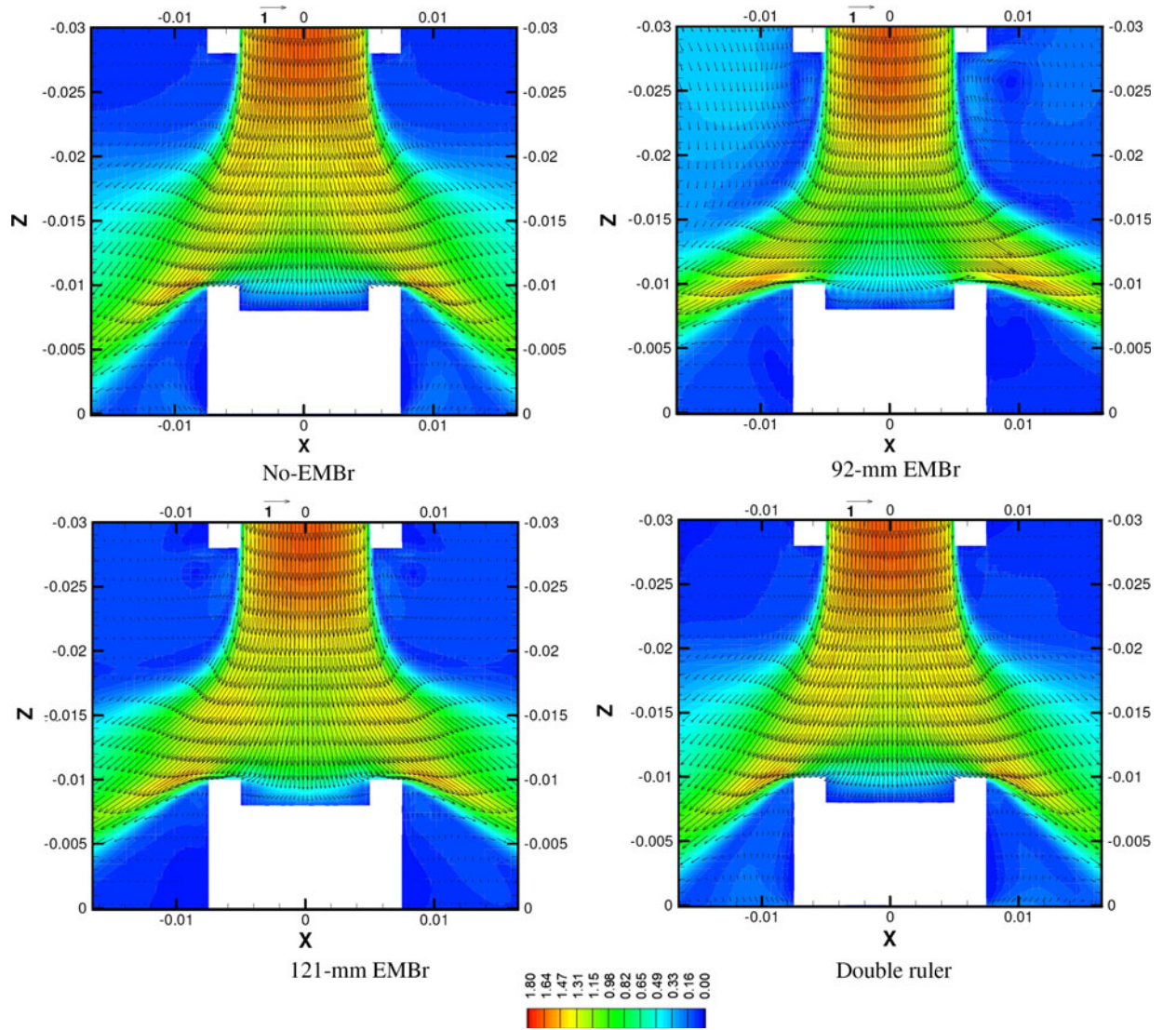


Fig. 8—Time-averaged velocity magnitude (m/s) contours and vectors near nozzle bottom in different cases.

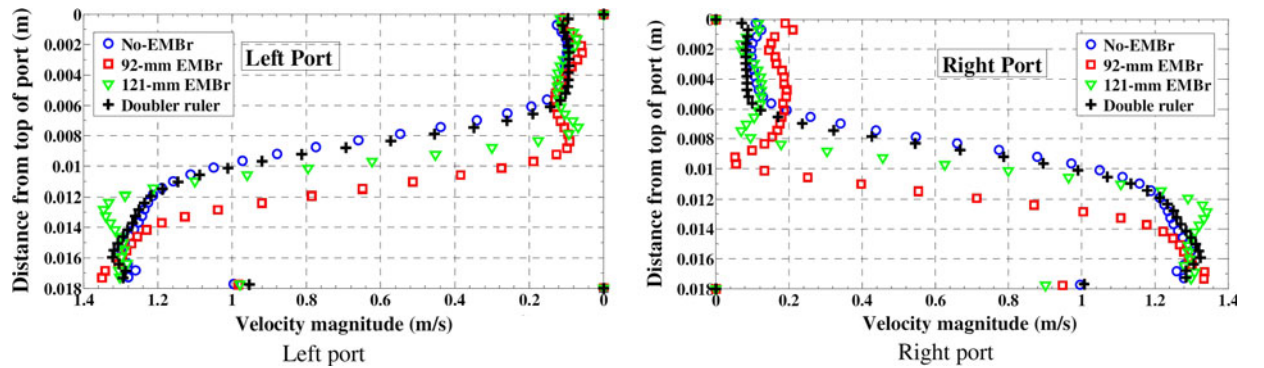


Fig. 9—Time-averaged velocity magnitude at port midplane vertical lines.

D. Turbulence Quantities

To investigate the effect of magnetic field on turbulence, the TKE budgets, TKE, and Reynolds stresses are presented in different parts of the nozzle and mold. The magnetic field interacts with the

instantaneous velocities, and both create and dissipate turbulent kinetic energy.^[28,29] The corresponding source and sink terms are added to the TKE transport equation because of the magnetic field normal to the wideface^[28,29]:

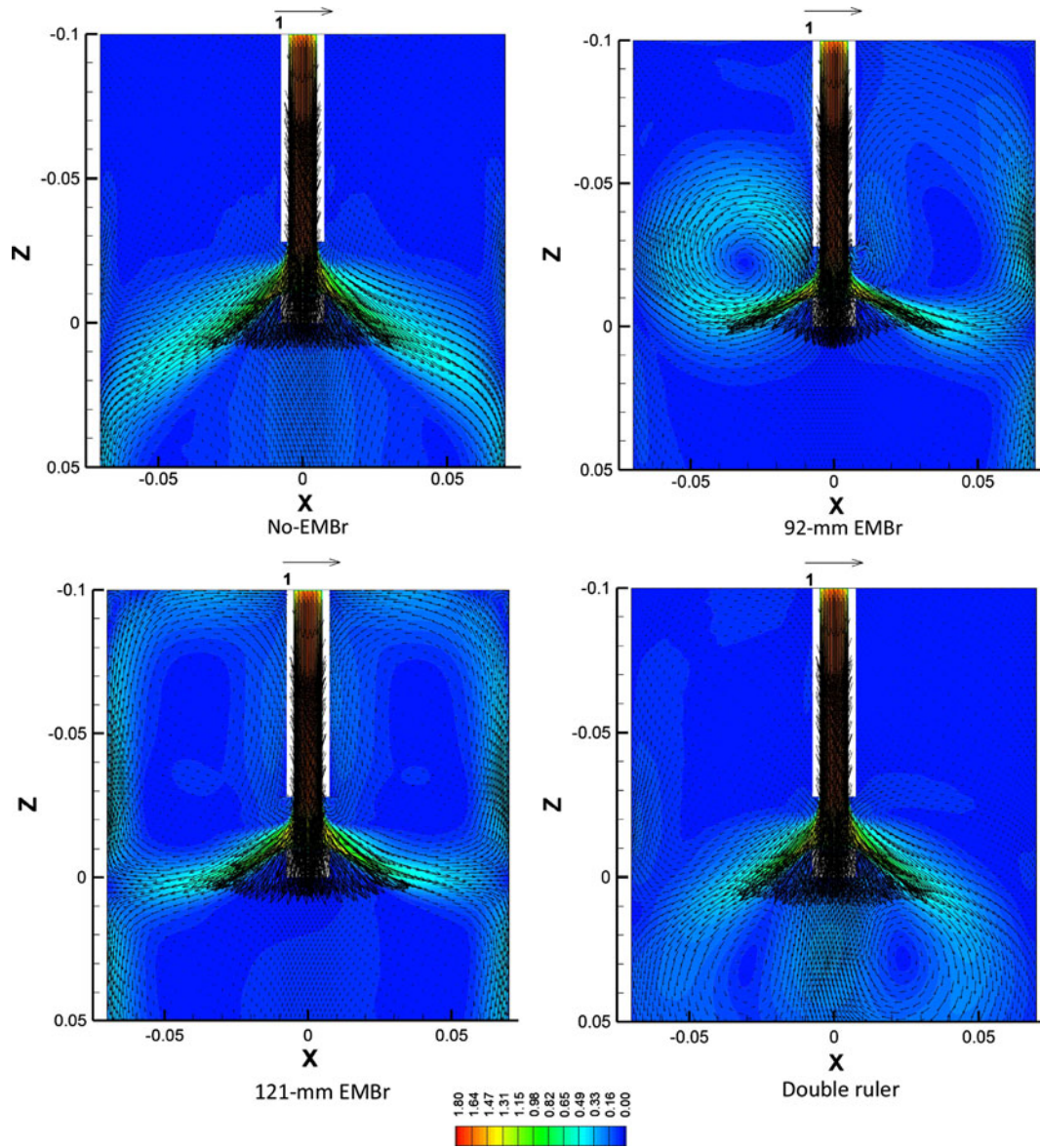


Fig. 10—Time-averaged velocity magnitude (m/s) contours and vectors at mold midplane in different cases. (Note: Vectors are skipped for clarity.).

$$\text{MHD source} = \frac{\sigma B_{0y}}{\rho} \left(\overline{u' \frac{\partial \phi'}{\partial z}} - \overline{w' \frac{\partial \phi'}{\partial x}} \right) \quad [8]$$

$$\text{MHD sink} = -\frac{\sigma B_{0y}^2}{\rho} \left(\overline{w'^2} + \overline{u'^2} \right) \quad [9]$$

Figure 12 presents these two terms and their sum for the different cases at the mold midplane between wide faces. As found previously in square and rectangular ducts,^[28,29] the sink terms are stronger than the source terms, thus causing net suppression of turbulence. The strongest suppression of turbulence is with 92-mm EMBr, where the magnetic field is strong across the nozzle well bottom and the jet region. In 121-mm EMBr

and double-ruler brake cases, the turbulence suppression effect is weaker.

Turbulent kinetic energy arises in the process because of the combined effects of turbulent flow and the magnetic field. Figure 13 shows the TKE along the vertical midlines of the ports and is symmetric between sides. The TKE is suppressed strongly by the 92-mm EMBr, followed by the 121-mm EMBr case. With the double-ruler brake, TKE is much higher, similar to the case with no EMBr. These results of increasing TKE match the progression of decreasing field strength across the nozzle in Figure 2(b). This quantifies how the magnetic field suppresses turbulence inside the nozzle.

Figures 14 and 15 present the TKE and its three components, the Reynolds normal stresses, in the mold midplanes. With weak magnetic fields across the nozzle

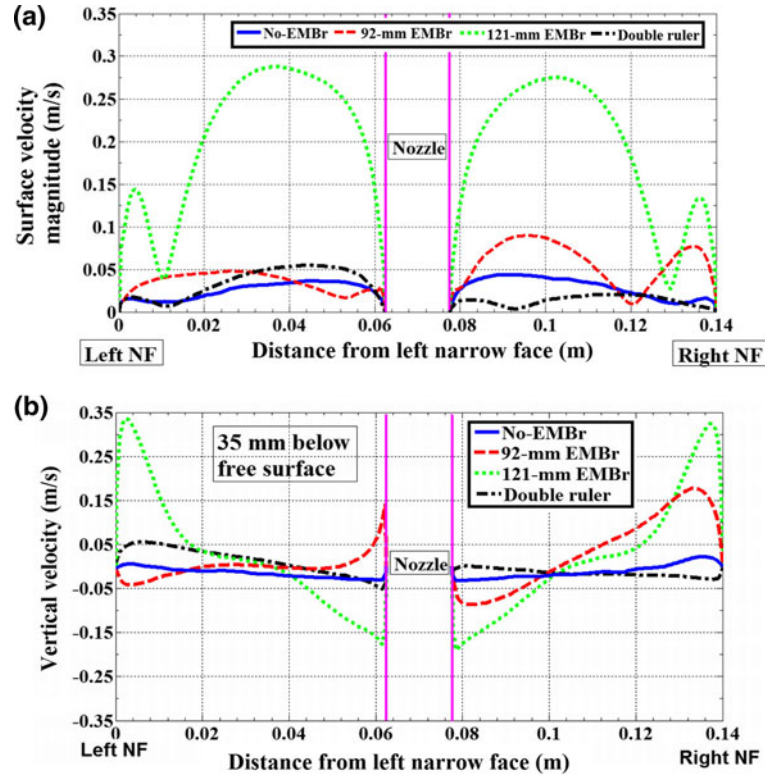


Fig. 11—(a) Horizontal surface velocity in different EMBR cases. (b) Vertical velocity (35 mm below free surface) in different EMBR cases. (Note: + ve vertical velocity is in upward direction).

bottom, the cases with no EMBR and a double-ruler brake sustain high turbulence within the nozzle bottom and ports. This is a result of rotating or “swirl” flow in the y - z plane of the nozzle bottom, which wobbles and oscillations in these two directions, as shown by the strong v' and w' components in Figure 15. Similar behavior was found in previous work with no EMBR.^[18] This alternating swirl is suppressed strongly by the single-ruler cases, with almost complete suppression by the 92-mm EMBR, which exerts the strongest magnetic field directly through/across the nozzle bottom.

Although all turbulence components are suppressed at the nozzle bottom well with the single-ruler cases (Figure 15), the horizontal components ($\overline{u'u'}$) persist in the mold because less turbulent mixing occurs in the nozzle, allowing large-scale variations to arise later in the mold cavity. With the 92-mm EMBR, high $\overline{u'u'}$ and TKE are observed even near the top surface, even though the velocities there are small. This finding suggests unstable transient variations in horizontal velocity (u') near the surface that are likely detrimental to steel quality. Reynolds shear stresses ($\overline{u'w'}$ and $\overline{v'w'}$) showed similar behavior with the intensity of the magnetic field and therefore are not presented here.

The turbulent kinetic energy at the free surface and 35 mm below is important to steel quality and is presented in Figures 16(a)-(b) for the different cases. The double-ruler brake shows similar low TKE as no-EMBr case, and it seems to have insufficient surface mixing to prevent meniscus freeing defects. The 92-mm

EMBr case experiences the highest TKE almost everywhere. The high turbulence levels and large right-left asymmetries with this ruler indicate detrimental unstable flow with long time periods, which makes the averaging time of 28 seconds insufficient.

On the left side surface, the TKE with the 121-mm EMBR is stronger, as expected from the higher surface velocity for this case. Moreover, this ruler maintains reasonable symmetric turbulence on both sides of the mold, both at the surface and at 35 mm below the surface. Thus, this ruler produces the best flow of the four cases for preventing surface defects in this case, as discussed previously.

VII. TRANSIENT RESULTS

The four LES model simulations reveal insights into the evolution of transient flow structures, which is more important for defect formation than averages. Sample instantaneous snapshots of the flow pattern, velocity fluctuation component histories, and a POD analysis are presented in this section.

A. Transient Flow Patterns

Figures 17(a) through (d) present a sequence of three instantaneous velocity magnitude snapshots spaced 1 second apart for each case, along with the corresponding time averages superimposed with magnetic

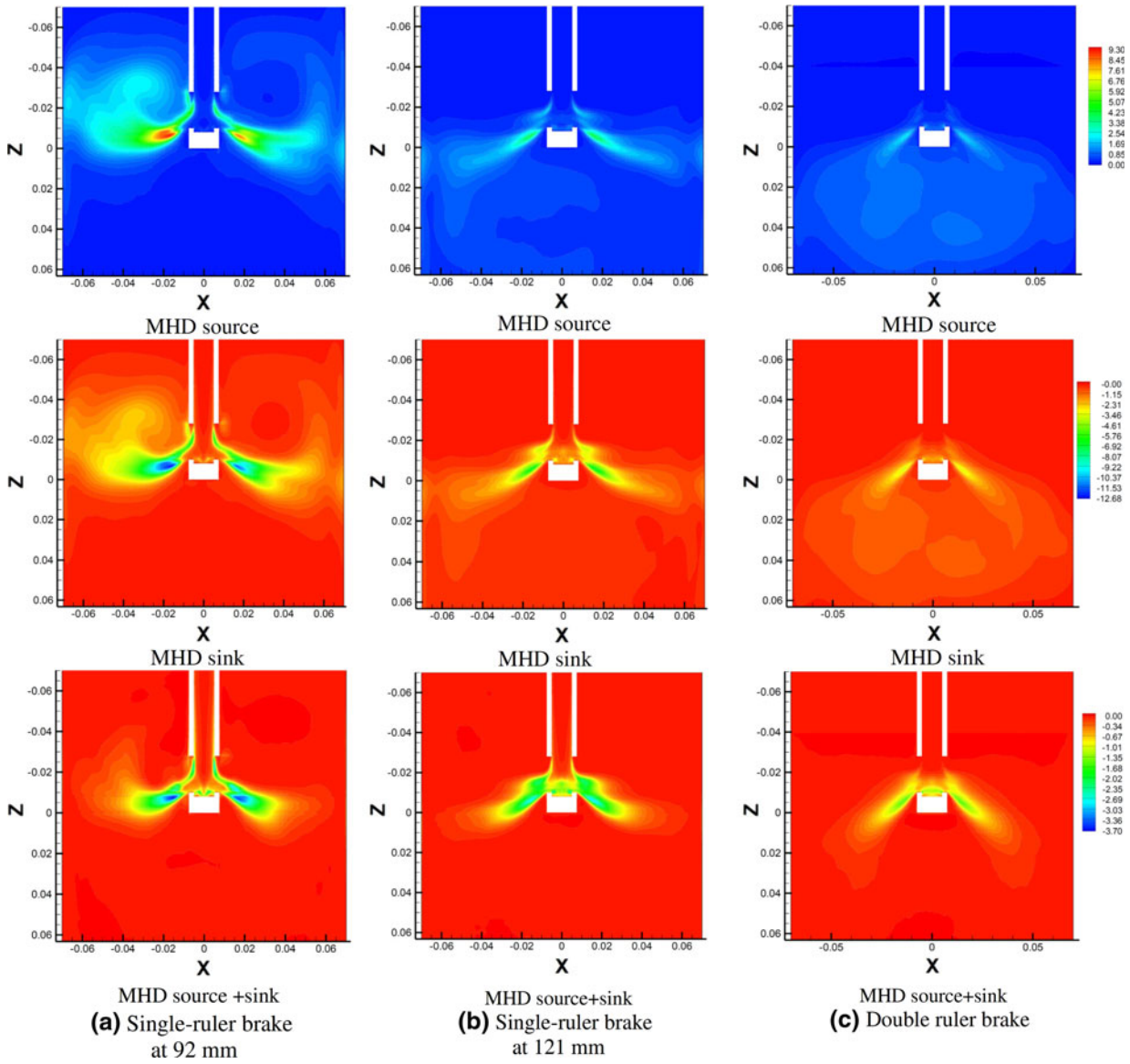


Fig. 12—Resolved MHD source, sink and net (source + sink) in TKE in different single/double-ruler brake cases.

field contours at the mold midplane between wide faces. Turbulence evolves differently in each case, so the snapshots (1 seconds apart) naturally do not correspond.

The no-EMBr snapshots are all similar and the flow variations are small with relatively high frequencies. The instantaneous flow fields are altered significantly by the magnetic field in the other three cases. Turbulence is suppressed in the direction (y -) of the magnetic field. This is especially noticeable at nozzle bottom. This turbulence suppression at nozzle bottom enables large-scale lower-frequency vortical structures to develop in the mold x - z plane. These large flow structures move into the upper- and lower-recirculation regions like unsteady laminar flows. This tends toward quasi 2-D turbulence with the strong magnetic field and insulated walls normal to the magnetic field. Similar behavior was reported by Timmel *et al.* in their measurements of this system.^[10,11] Others have also reported turbulent flow growing large-scale

vortical cylindrical structures with axes aligned with the strong magnetic field.^[34] In this condition, the viscous and magnetic dissipation of turbulence decreases and large scale variations dominate.^[34]

With different magnetic fields, the transient flow behavior changes greatly. With 92-mm EMBr, the magnetic field is strongest across the port region and laminarizes flow in the nozzle bottom, which leads to large-scale structures with low-frequency oscillations dominating flow variations in the mold cavity. The left-side jet forms a circular roll spanning half of the mold width next to the port, whereas the right-side jet hits the narrow face and splits partly upward toward the surface and partly downward. This behavior flips between the right and left sides with low frequencies (<0.02 Hz). Because the jets enter the mold into the strongest part of the magnetic field, a randomly high jet tends to be deflected upward, whereas a low jet tends to be deflected

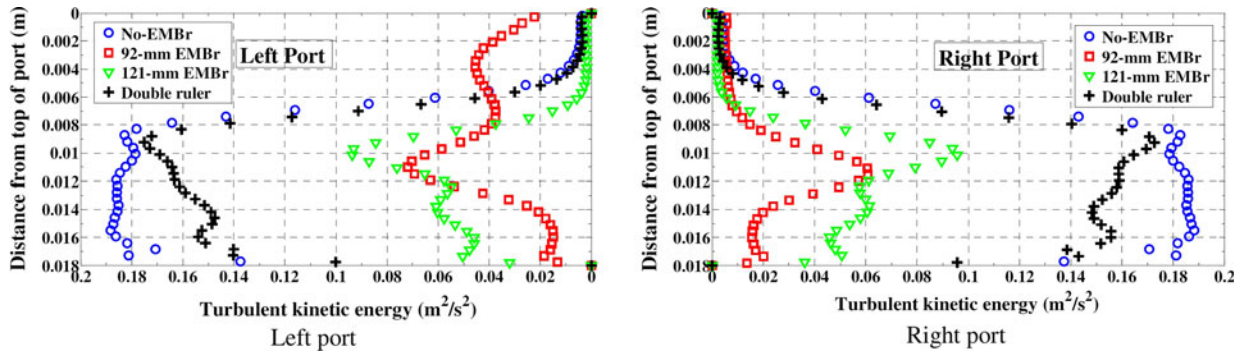


Fig. 13—Resolved turbulent kinetic energy along centerline of port outlet plane.

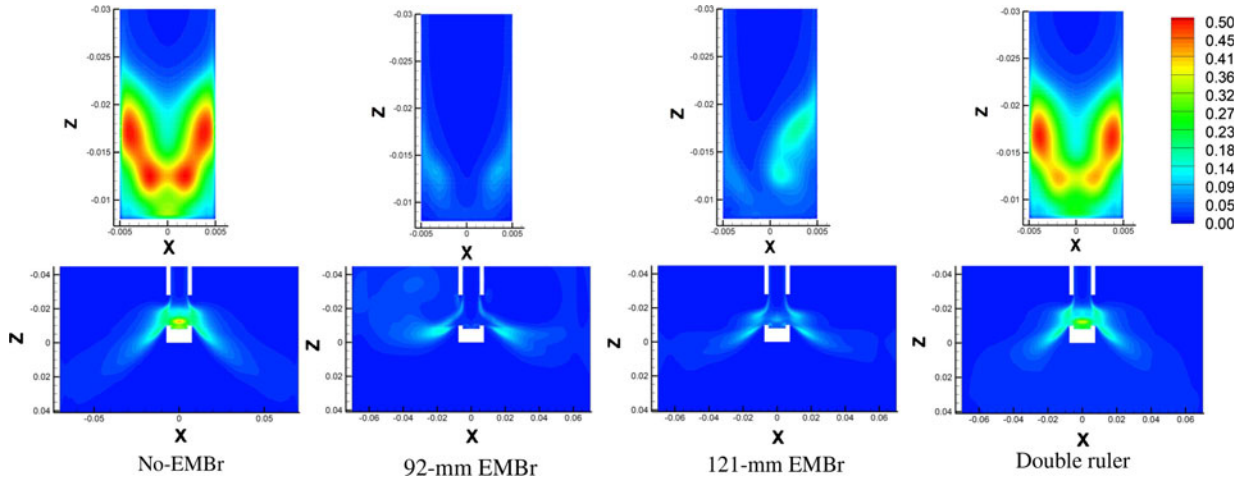


Fig. 14—Turbulent kinetic energy (m^2/s^2) at mold midplanes between wide faces. (below) and between narrow faces inside nozzle (above) for four different cases.

downward. This mechanism acts to amplify flow variations and produces the most unstable flow behavior of all the cases.

Lowering the ruler brake by 29 mm (121-mm EMBR) weakens the magnetic field across the nozzle well, so the exiting jets contain more high-frequency turbulence. The increased turbulent swirl within the nozzle bottom stabilizes the jet so the strength of the large-scale variations is reduced and the mold flow structures are small. In addition, the magnetic field below the jet applies more deflection force to lower jets randomly than it does to higher jets. This stabilizing mechanism leads to reasonably symmetric flow in the mold after 28 seconds. With a perfectly symmetric magnetic field, symmetry was achieved even faster, within only ~ 5 seconds of time averaging.

With the double-ruler brake, the magnetic field across the nozzle bottom is smallest so turbulence is suppressed only weakly. The strongly mixed, downward-angled jet penetrates below the magnetic field region. In the lower region, the flow then recirculates with large-scale, slowly evolving flow structures, which alternate between the left and right. Flow up the narrow faces also flips on both sides with time. The turbulence scales and time scales of

the flow asymmetries are intermediate between those of the 92-mm and 121-mm EMBR cases.

B. Anisotropic Suppression of Turbulence

To further reveal how magnetic field suppresses turbulence in the nozzle bottom and elsewhere in the mold, Figure 18(a) presents the three components of velocity fluctuation as a function of time at the nozzle bottom center (P-1 in Figure 5) for the different cases. The ~ 3 to 4 Hz alternation of v' signifies the alternating direction of swirl in the nozzle bottom. This frequency agrees with previous work without EMBR.^[18] The other velocity components at this location fluctuate at higher frequencies. Note that the strong magnetic field of the 92-mm and 121-mm EMBR cases suppresses almost all velocity fluctuations at this point. It is particularly interesting that the velocity fluctuation component parallel to the magnetic field (v') is suppressed the most strongly. This anisotropic suppression of turbulence effectively prevents swirl in the nozzle bottom. This leads to a smoother, but less-stable jet leaving the ports that is partly responsible for the large-scale variations in the mold, as discussed previously.

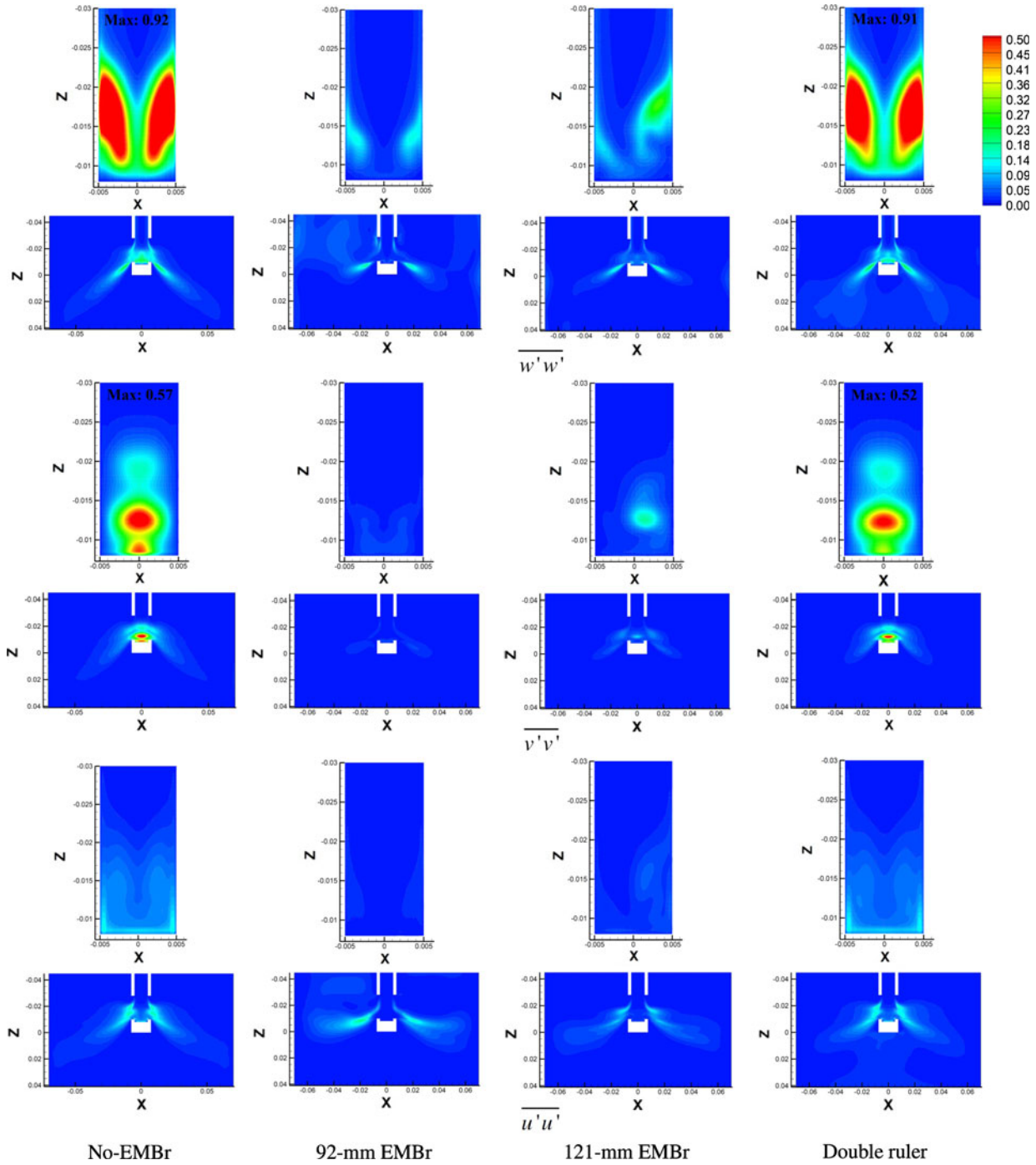


Fig. 15—Resolved Reynolds stresses (m^2/s^2) at mold midplanes between wide faces (below) and between narrows faces inside nozzle (above) for four different cases.

The three velocity-fluctuation components at the mold midplane at points near the left port exit and near the mold center (P-6 and P-5 in Figure 5, respectively) are shown in Figures 18(b) and (c), respectively. At the port exit, v' shows similar positive–negative alternation at ~ 3 to 4 Hz as found at nozzle bottom for the no-EMBr and double-ruler cases. This observation indicates that the alternating swirling flow of the jet extends into the mold. This effect diminishes with distance from the port and is not viewed near the mold

center. For all three cases, the high-frequency velocity variations decrease from port exit to the mold interior, but the increasing difference between the components reveals that the turbulence becomes more anisotropic, as large-scale structures start to develop in the x - z plane.

C. POD Analysis

A POD of the velocity fluctuation predictions for the different cases has been performed using single value

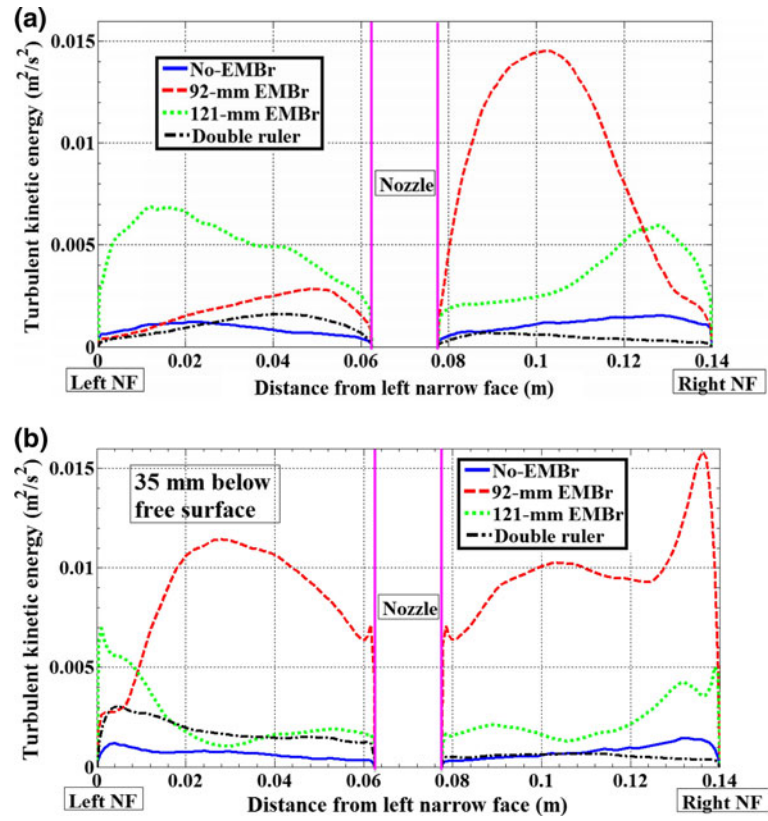


Fig. 16—(a) Resolved turbulent kinetic energy at surface in different cases. (b) Resolved turbulent kinetic energy at 35 mm below the free surface in different cases.

decomposition as described in our previous work.^[18] The POD analysis splits the velocity fluctuations into orthonormal spatial modes and corresponding temporal coefficients. The 2000×57900 POD data matrix $[U'_z]$, was based on $193(x-) \times 100(z-)$ spatial values for each velocity component over 12 seconds with a 0.006-second time interval. The POD results are another way to visualize the transient velocity variations presented in Sections VII-A and VII-B.

Figure 19 compares the first two mode shapes for the EMBR cases. The significant modes for no-EMBr case were presented in our previous work.^[18] Without EMBR, the first and second (v') mode shapes in the bottom of the nozzle port were the strongest and represented the alternating direction of the swirling flow.^[18] The other (u' and w') components were small. The double-ruler and 121-mm EMBR cases have similar v' modes, except they are progressively weaker because of the increasing strength of the magnetic field across the nozzle bottom. This flow-variation mode is completely absent in the 92-mm EMBR case because the strong field suppresses the swirl flow in the nozzle completely.

The 92-mm EMBR, shows strong POD modes in the mold interior. Specifically, the first mode has regions of strong variations in horizontal velocity (u') on the right side, and the second mode has variations in vertical velocity (w') on the left. These two in-plane variations reveal the large-scale flow structures observed in Figure 17. Specifically, the right jet wobbles vertically,

and the left flow roll oscillates horizontally, as flow in the upper recirculation region wanders continuously and evolves with time.

With its magnetic field lowered below the nozzle, the 121-mm EMBR experiences many different flow-variation modes, including weak nozzle swirl, and weakened modes in the mold interior that are similar to the 92-mm case. The horizontal (u') first mode of jet wobbling is closer to the nozzle than with 92-mm EMBR and the two x - z plane second modes (u' and w') are weaker and more symmetrical.

With the double-ruler EMBR, the weak magnetic field across the nozzle bottom region allows swirl to be sustained inside the nozzle, producing first-mode v' regions similar to the no-EMBr case. The second mode shows significant x - z plane flow variations in vertical (w') and horizontal (u') because of the complex alternating flow rolls below the nozzle.

Although the first two modes are the most important, each evolving flow pattern is actually complex and includes more than 1000 important modes. Figure 20 presents the cumulative energy contained in the different modes for different cases. The 121-mm EMBR curve has the slowest progression as its energy is spread across more scales because its flow pattern contains the most different important flow-variation structures, as observed previously. Its first two modes contain 14.7 pct of the total energy. The first two modes with 92-mm EMBR are even more dominant, containing 31 pct of the energy, which

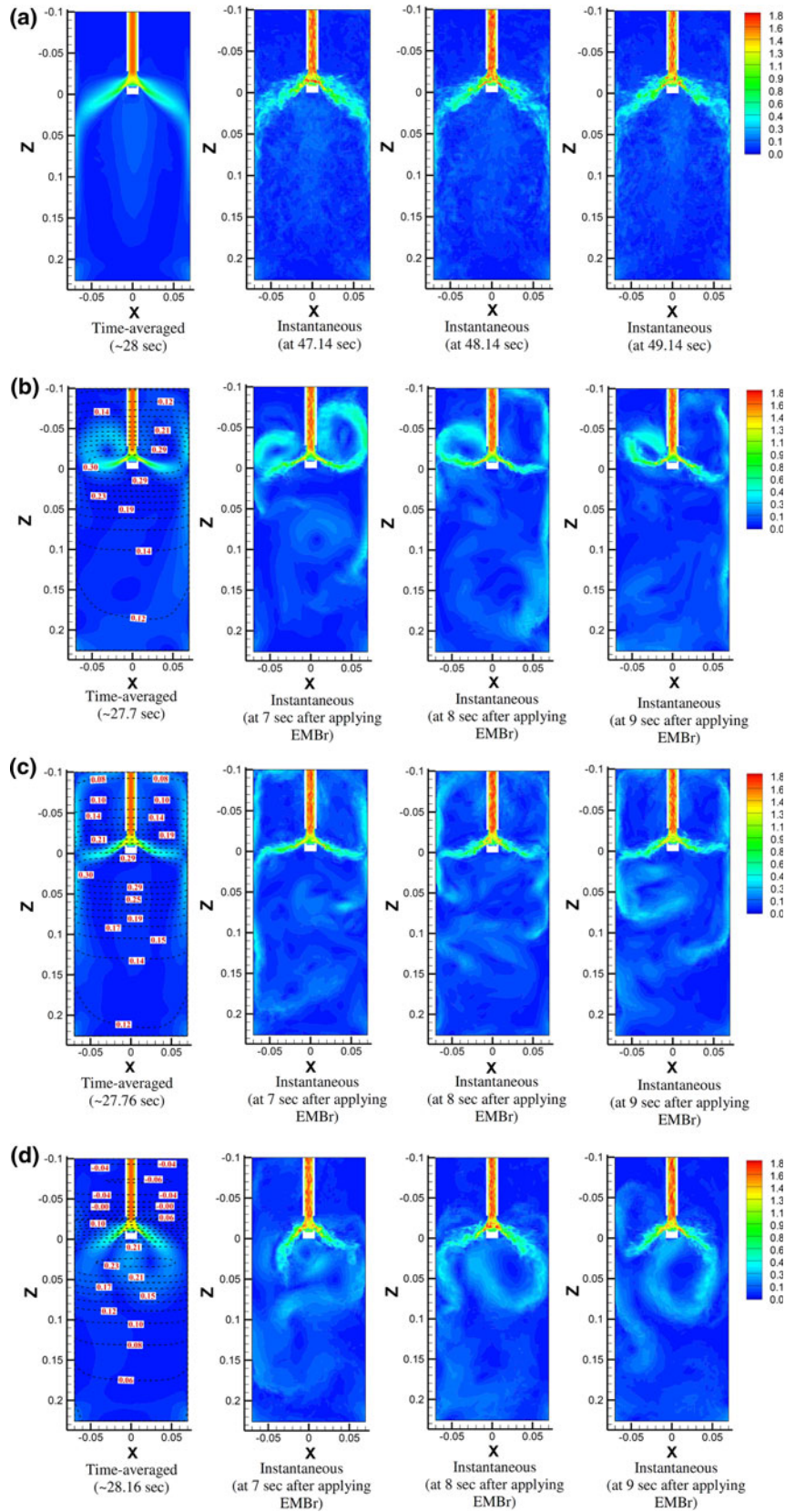


Fig. 17—Time-averaged and instantaneous velocity magnitude (m/s). (a) No EMBr ($t = 0$ is the zero velocity field in the whole domain) (b) 92-mm EMBr (c) 121-mm EMBr (d) Double-ruler EMBr (In EMBr cases, brake is applied at $t = 49.14$ s on developed no-EMBr flow field).

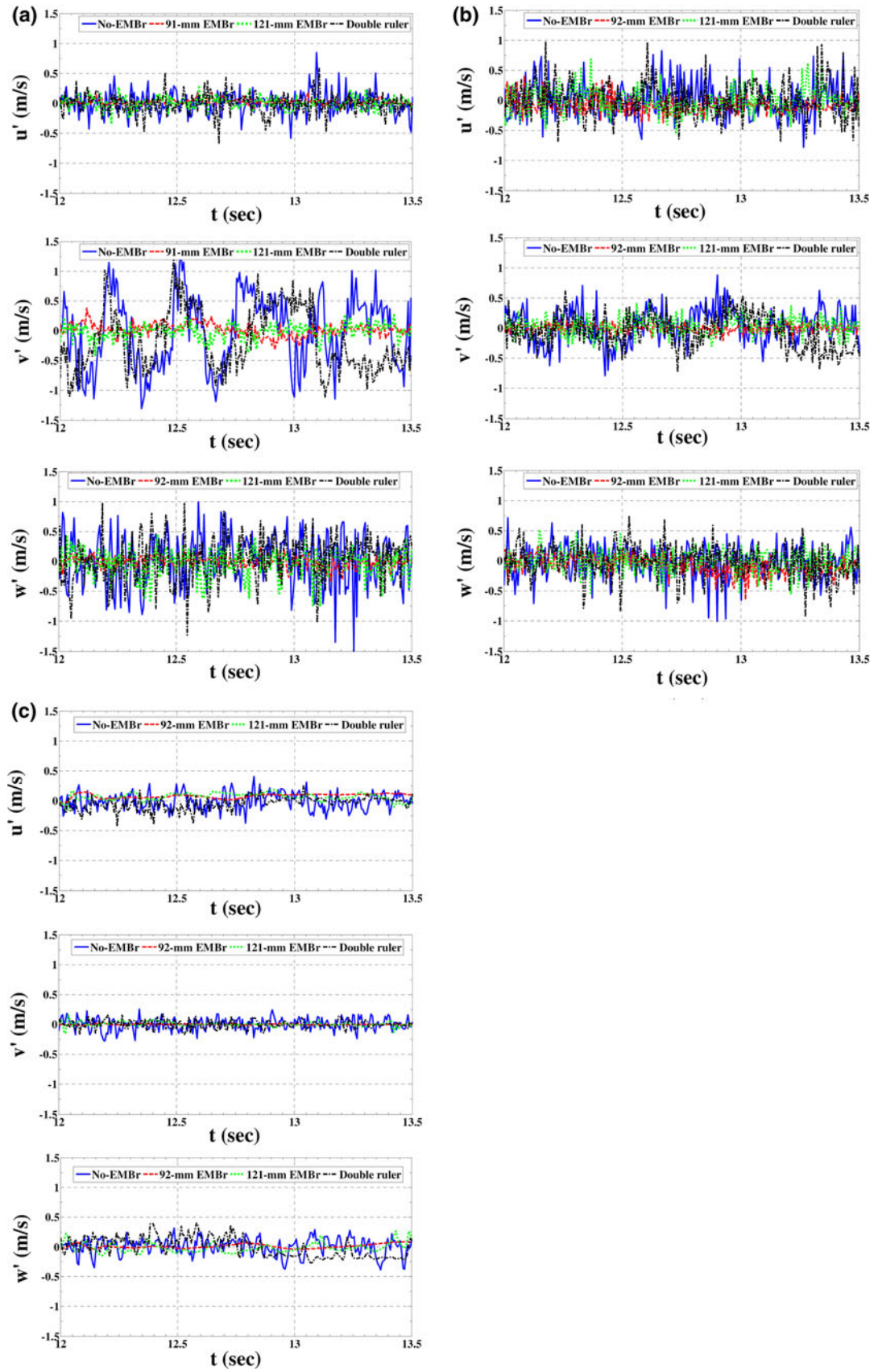


Fig. 18—Three components of instantaneous velocity fluctuations at mold midplane in different cases (a) At P-1 (b) At P-6 (c) At P-5 (as shown in Fig. 5).

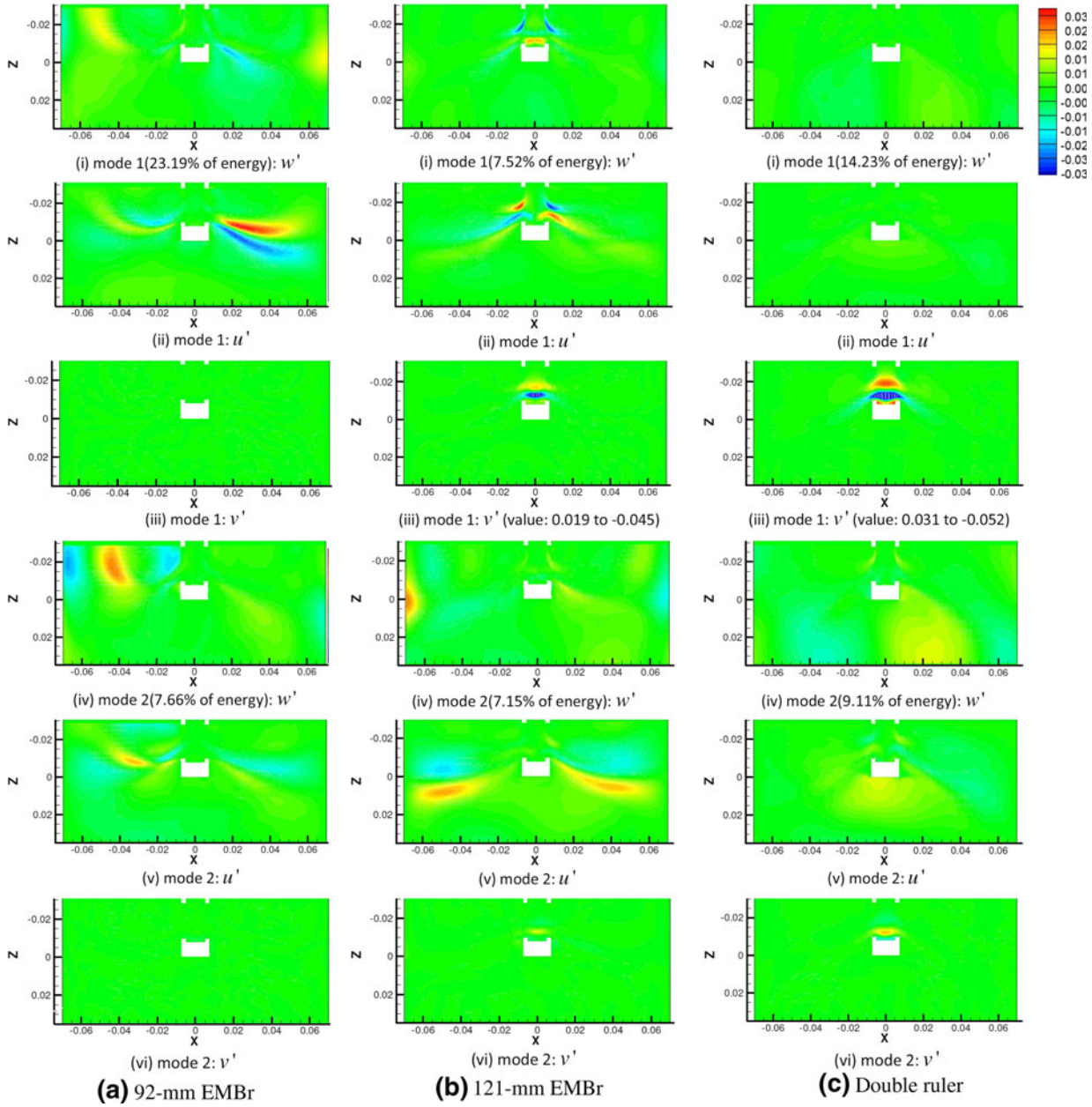


Fig. 19—First two modes with corresponding velocity fluctuations.

indicates the strong nature of the unstable oscillating flow structures in the upper mold interior. The first two modes of the no-EMBr and double-ruler cases contain 22.2 and 23.5 pct, respectively. This indicates the strong nature of the swirling flow mode in the nozzle.

To understand the transient behavior of these modes, Figure 21 shows how the temporal coefficients of the first four modes vary with time, for 6 sec. The variations oscillate between positive and negative, as noted previously.^[18] The variations contain both low and high frequencies. The temporal coefficients with 92-mm EMBR showed the strongest low-frequency variations, whereas those with no EMBR showed the highest. These variations are consistent with the behavior of the corresponding modes already discussed.

VIII. SUMMARY AND CONCLUSIONS

The current work investigates the effect of EMBR on turbulent flow in the nozzle and mold during continuous casting of steel slabs using four transient large eddy simulations. The computations reasonably match both time-average and filtered transient histories of ultrasonic Doppler velocimetry measurements in a small-scale GaInSn model of the studied geometry, including two single-ruler EMBR cases, and a no-EMBr case studied previously.^[18] In addition, the model can capture high-frequency velocity fluctuations and velocities near the SEN and NF, which are missed by the measurements. The following effects of electromagnetic braking on transient and time-average flow fields are observed:

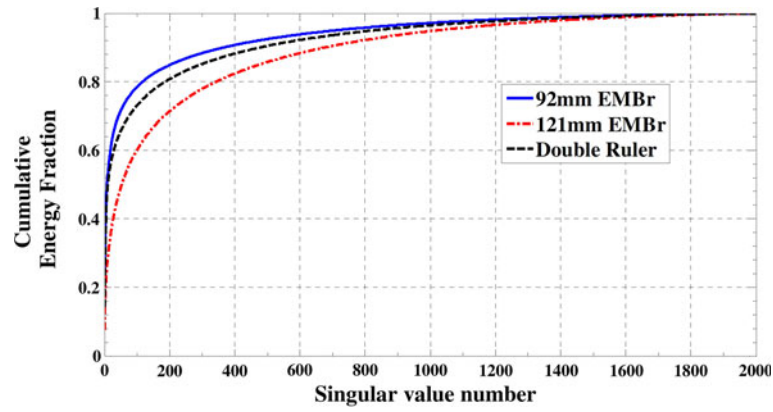


Fig. 20—Cumulative energy fraction with increasing number of modes included.

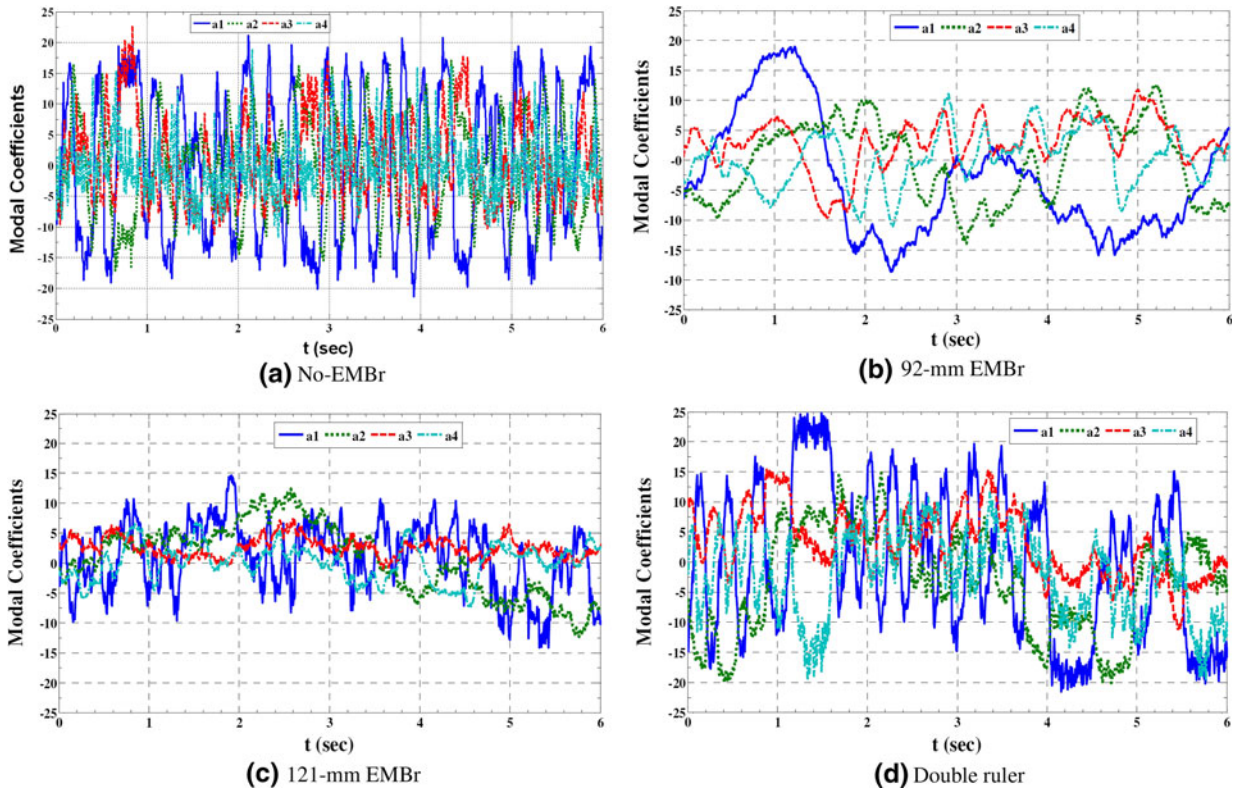


Fig. 21—Temporal coefficients of first four modes in different cases.

- Applying a magnetic field suppresses turbulence. This is especially important across the nozzle bottom, where a strong magnetic can prevent the alternating swirling flow that otherwise develops with an oscillation frequency of 3 to 4 Hz. The resulting jets exiting the ports are straight, thin, and laminarized.
- The region of the strongest magnetic field tends to deflect the jet away. This leads to more upward-directed flow for the 121-mm EMBR positioned below the nozzle, more downward-directed flow for the double-ruler EMBR, and unstable flow for the 92-mm EMBR positioned directly across the nozzle.
- Applying a magnetic field across the nozzle leads to unstable large-scale, low-frequency time-varying vortical structures in the x-z plane of the upper and lower recirculation regions in the mold, whose axes are aligned with the magnetic field.
- This tendency of the vortices toward 2-D turbulence agrees with previous work, including measurements by Timmel *et al.*^[10,11] of this system.
- The symmetry of the magnetic field becomes important for the unstable case with a strong magnetic field applied across the port and jet regions. Slight asymmetry between the right and left sides of the magnetic

field causes asymmetric flow structures in the mold to persist for long periods.

- Moving the magnetic field below nozzle bottom deflects the jet upward, leading to a shallower downward jet angle and higher surface velocity. Furthermore, this method allows the jet to retain its turbulence, and related mixing, leading to more stable flow in the mold. For a deep nozzle submergence, this practice has the potential to provide sufficient surface flow and mixing to avoid quality problems related to meniscus freezing.
- The flow variations contain more energy in larger, low-frequency scales for the 92-mm EMBr across the nozzle. Without EMBr or with the double-ruler brake, more turbulent energy is contained in the high-frequency nozzle swirl. The 121-mm EMBr case has flow variation energy distributed over many different flow modes.
- With insulated walls (no steel shell), this work finds that flow is most stable without EMBr.

Overall, this work shows the importance of the location and strength of electromagnetic braking in both the continuous casting nozzle and mold. Positioning the strongest magnetic fields across the nozzle bottom and port regions leads to detrimental unstable flow, so this practice should be avoided. Magnetic fields can be used to increase or decrease surface velocity and turbulence, giving them the potential to control flow-related defects if optimized. Subsequent work is needed to investigate and quantify the stabilizing effect of the current-conducting solidifying steel shell on the flow.

ACKNOWLEDGMENTS

The authors are grateful to K. Timmel, S. Eckert, and G. Gerbeth from MHD Department, Forschungszentrum Dresden-Rossendorf (FZD), Dresden, Germany for providing the velocity measurement database and complete conditions for the GaInSn model experiments. This work was supported by the Continuous Casting Consortium, Department of Mechanical Science & Engineering, University of Illinois at Urbana-Champaign, IL, and the National Science Foundation, Grant CMMI 11-30882. Also, we would like to thank Silky Arora for helping us with data extraction codes for the POD analysis.

REFERENCES

1. B.G. Thomas: *Casting Volume*, 11th ed., vol. 5, AISE Steel Foundation, A. Cramb, ed., Pittsburgh, PA, 2003, pp. 14.1–14.41.
2. L.C. Hibbeler, R. Liu, and B.G. Thomas: *Proc. 7th European Conf. on Continuous Casting*, Dusseldorf, Germany, 2011.

3. B.G. Thomas and L. Zhang: *ISIJ Int.*, 2001, vol. 41 (10), pp. 1181–93.
4. K. Cukierski and B.G. Thomas: *Metall. Mater. Trans. B*, 2008, vol. 39B, pp. 94–107.
5. J. Nakashima, J.A. Kiyose, Y. Ohtani, J. Fukuda, T. Kawase, and M. Doki: Nippon Steel Technical Report No. 86, Nippon Steel, 2002, No. 86, pp. 61–67.
6. H.R. Hackl, A.F. Lehman, J.E.A. Eriksson, and S.G. Kollberg: *AISTech Preliminary Program*, AIST, Warrendale, PA, 2006.
7. K. Okazawa, T. Takehito, J. Fukuda, T. Kawase, and M. Toki: *ISIJ Int.*, 2001, vol. 41 (8), pp. 851–58.
8. P.H. Dauby and S. Kunstreich: *Ironmaking Steelmaking*, 2005, vol. 32 (1), pp. 80–86.
9. M. Zeze, H. Harada, E. Takeuchi, and T. Ishii: *76th Steelmaking Conf*, Dallas, TX, 1993, pp. 267–72.
10. K. Timmel, S. Eckert, and G. Gerbeth: *Metall. Mater. Trans. B*, 2011, vol. 42B, pp. 68–80.
11. K. Timmel, X. Miao, S. Eckert, D. Lucas, and G. Gerbeth: *Magnetohydrodynamics*, 2010, vol. 46 (4), pp. 337–448.
12. Y. Hwang, P. Cha, H. Nam, K. Moon, and J. Yoon: *ISIJ Int.*, 1997, vol. 37 (7), pp. 659–67.
13. R.H.M.G. Nabben, R.P.J. Duursma, A.A. Kamperman, and J.L. Lagerberg: *Ironmaking Steelmaking*, 1998, vol. 25 (5), pp. 403–06.
14. M.Y. Ha, H.G. Lee, and S.H. Seong: *J. Mater. Process. Technol.*, 2003, vol. 133 (3), pp. 322–39.
15. K. Takatani, K. Nakai, N. Kasai, T. Watanabe, and H. Nakajima: *ISIJ Int.*, 1989, vol. 29 (12), pp. 1063–68.
16. M. Yao, M. Ichimiya, M. Tamiya, K. Suzuki, K. Sugiyama, and R. Mesaki: *Trans. Iron Steel Inst. Japan*, 1984, vol. 24 (2), p. s211.
17. Q. Yuan, B.G. Thomas, and S.P. Vanka: *Metall. Mater. Trans. B*, 2004, vol. 35B, pp. 685–702.
18. R. Chaudhary, C. Ji, B.G. Thomas, and S.P. Vanka: *Metall. Mater. Trans. B*, 2011, vol. 42B, pp. 987–1007.
19. X. Huang and B.G. Thomas: *Can. Metall. Q.*, 1998, vol. 37 (3–4), pp. 197–212.
20. Z.-D. Qian and Y.-L. Wu: *ISIJ Int.*, 2004, vol. 44 (1), pp. 100–07.
21. R. Kageyama and J.W. Evans: *ISIJ Int.*, 2002, vol. 42 (2), pp. 163–70.
22. Y. Miki and S. Takeuchi: *ISIJ Int.*, 2003, vol. 43 (10), pp. 1548–55.
23. K. Timmel, S. Eckert, G. Gerbeth, F. Stefani, and T. Wondrak: *ISIJ Int.*, 2010, vol. 50 (8), pp. 1134–41.
24. S.B. Pope: *Turbulent Flows*, Cambridge University Press, Cambridge, UK, 2000.
25. J.O. Hinze: *Turbulence*, McGraw-Hill Publishing Company, New York, NY, 1975.
26. F. Nicoud and F. Ducros: *Flow, Turbulence, Combustion*, 1999, vol. 63 (3), pp. 183–200.
27. R. Moreau: *Magnetohydrodynamics*, Kluwer Academic Pub. Co., Norwell, MA, 1990, pp. 110–64.
28. R. Chaudhary, S.P. Vanka, and B.G. Thomas: *Phys. Fluids*, 2010, vol. 22, p. 075102.
29. R. Chaudhary, A.F. Shinn, S.P. Vanka, and B.G. Thomas: *Comput. Fluid*, 2011, vol. 51 (1), pp. 100–14.
30. M.H. Baba-Ahmadi and G. Tabor: *Comput. Fluid*, 2009, vol. 38 (6), pp. 1299–311.
31. H. Werner and H. Wengle: *8th Symposium on Turbulent Shear Flows*, Munich, Germany, 1991.
32. A. Sohankar, C. Norberg, and L. Davidson: *Int. J. Num. Meth. Fluids*, 1998, vol. 26, pp. 39–56.
33. R. Chaudhary, G.-G. Lee, B.G. Thomas, and S.-H. Kim: *Metall. Mater. Trans. B*, 2008, vol. 39B, pp. 870–84.
34. R. Moreau: *Why, How and When MHD Turbulence Becomes Two-Dimensional, Liquid Metal Flows and Magnetohydrodynamics, Progress in Astronautics and Aeronautics*, vol. 84, H. Branover, P.S. Lykoudis, and A. Yakhot, eds., American Institute of Aeronautics and Astronautics, Inc., New York, NY, 1981.